Formation of a metamorphic complex along an obliquely convergent margin: Structural and thermochronological evolution of the Chugach Metamorphic Complex, southern Alaska

Deta Gasser,[1,2] Emilie Bruand,[1] Kurt Stüwe,[1] David A. Foster,[3] Ralf Schuster,[4] Bernhard Fügenschuh,[5] and Terry Pavlis[6]

Received 5 August 2010; revised 7 January 2011; accepted 20 January 2011; published 20 April 2011.

[1] This study documents the structural and metamorphic evolution of middle to lower crust along an oblique convergent curved continental margin during a time span of ~60 Myr. Our study documents the importance of variable obliquity during convergence which led to the development of overprinting fabrics and distinct exhumation histories along strike of the margin. We present structural analyses, $^{40}Ar/^{39}Ar$, Rb/Sr, and zircon fission track ages from middle to lower crust exposed along the southern Alaskan margin in the Chugach Metamorphic Complex. Together with the metamorphic history and additional geochronology from the literature we derive the following tectonic evolution for this area: accretion of sediments during dextrally oblique convergence led to strain-partitioned D_1 structures and greenschist-facies metamorphism prior to circa 55 Ma. At ~55–51 Ma, a margin-parallel stretching phase with vertical thinning (D_2) affected the margin and led to andalusite-sillimanite grade metamorphism and the onset of partial melting. A switch back to dextral transpression (D_3) shortly after D_2 led to rapid cooling of the western and central parts of the complex associated with exhumation of parts of the core of the complex until circa 46 Ma. The southeastern part of the complex cooled and exhumed regularly and slowly until circa 5 Ma due to its highly oblique orientation relative to the convergence direction. An increase in cooling and exhumation occurred after circa 5 Ma in the entire southeastern part of the complex, associated with the Neogene collision of the Yakutat terrane.

Citation: Gasser, D., E. Bruand, K. Stüwe, D. A. Foster, R. Schuster, B. Fügenschuh, and T. Pavlis (2011), Formation of a metamorphic complex along an obliquely convergent margin: Structural and thermochronological evolution of the Chugach Metamorphic Complex, southern Alaska, *Tectonics*, *30*, TC2012, doi:10.1029/2010TC002776.

1. Introduction

[2] Oblique convergence between two lithospheric plates is common in ancient and active orogenic belts all over the world [e.g., *Teyssier et al.*, 1995; *Whitney et al.*, 2007; *Abu-Alam and Stüwe*, 2009; *Foster et al.*, 2009; *Goscombe and Gray*, 2009]. The resulting deformation between the two moving regions is generally termed transpression [e.g., *Sanderson and Marchini*, 1984]. The fabric development, the metamorphic evolution and exhumation history in such a transpressional region may differ considerably from orogen-normal systems, and factors such as the rate and obliquity of convergence, the ratio between simple and pure shear, the inclination and frictional properties of the bounding shear zones and spatially focused erosion may play an important role [e.g., *Fossen and Tikoff*, 1993; *Robin and Cruden*, 1994; *Tikoff and Teyssier*, 1994; *Jones et al.*, 1997; *Thompson et al.*, 1997; *Teyssier and Tikoff*, 1999; *Czeck and Hudleston*, 2003; *Schulmann et al.*, 2003; *Koons et al.*, 2003; *Jones et al.*, 2004]. The southern margin of Alaska has been controlled by overall oblique convergence between oceanic plates of the Pacific basin and the continental part of the North American plate throughout the Cenozoic [e.g., *Plafker et al.*, 1994]. It therefore represents an ideal natural laboratory to investigate the structural and metamorphic evolution of orogenic crust along a transpressional plate margin.

[3] In this contribution we present the results of a multi-disciplinary study conducted on a metamorphic complex formed along this obliquely convergent margin: the Chugach Metamorphic Complex (CMC) (Figure 1 [*Hudson and Plafker*, 1982; *Sisson et al.*, 1989; *Pavlis and Sisson*, 1995, 2003]). The CMC is a 10–50 km wide and ~350 km long upper amphibolite facies metamorphic complex which developed during the Eocene in the Late Cretaceous to Paleocene

[1]Department of Earth Science, University of Graz, Graz, Austria.
[2]Department of Geosciences, University of Oslo, Oslo, Norway.
[3]Department of Geological Sciences, University of Florida, Gainesville, Florida, USA.
[4]Geological Survey of Austria, Vienna, Austria.
[5]Faculty of Geo- and Atmospheric Sciences, University of Innsbruck, Innsbruck, Austria.
[6]Department of Geological Sciences, University of Texas at El Paso, El Paso, Texas, USA.

0278-7407/11/2010TC002776

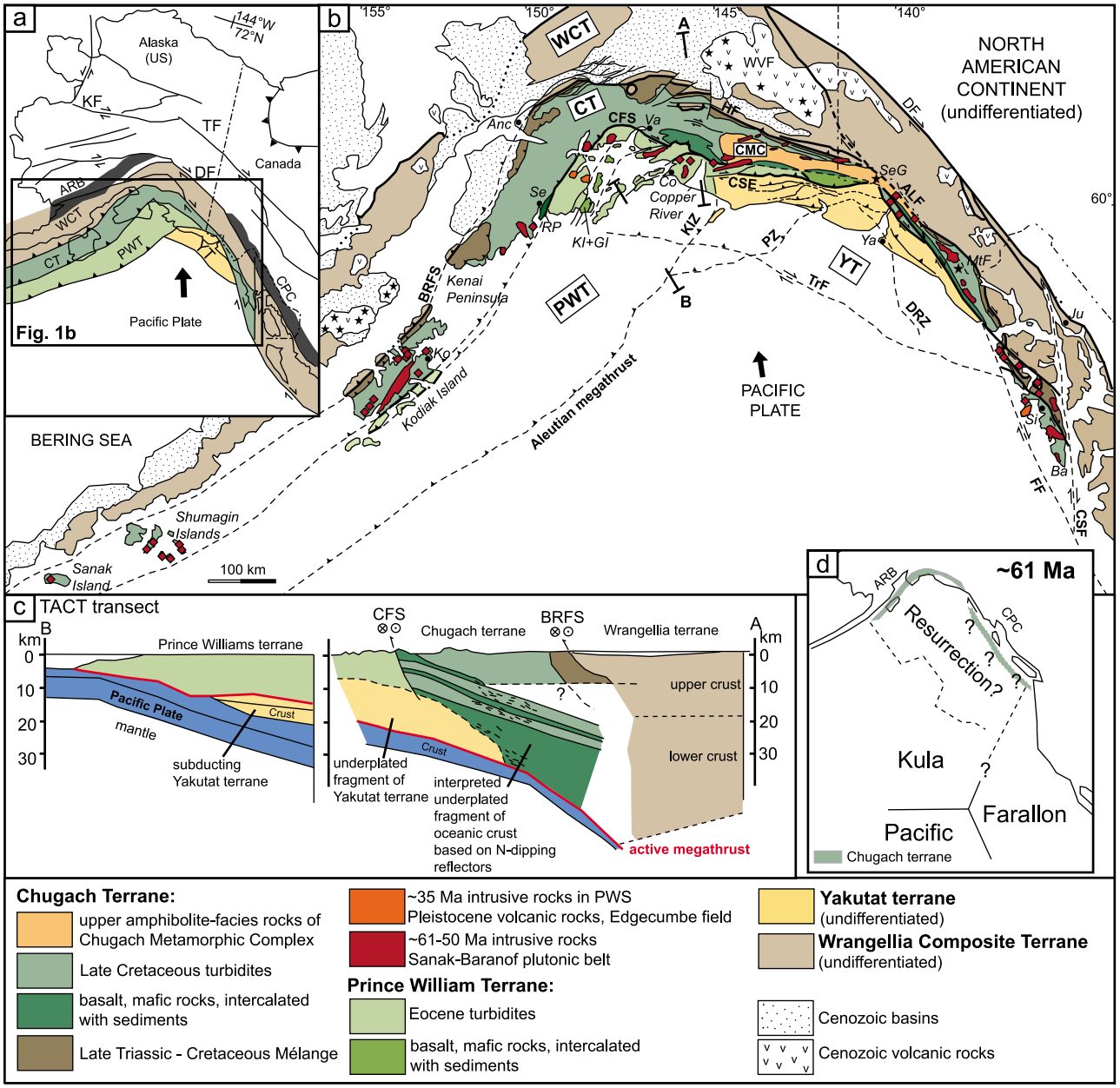

Figure 1. (a) Tectonic sketch map of Alaska showing the location of the tectonic terranes relevant for this study and major Neogene faults of the northern Cordillera. (b) Geological map of the southern Alaska margin, modified from *Plafker et al.* [1994], and faults of the Border Range Fault System after *Pavlis and Roeske* [2007]. (c) Crustal profile through the southern Alaska margin, along the Trans-Alaska Crustal Transect (TACT) route, after *Fuis et al.* [2008] and *Fuis and Plafker* [1991]. (d) Schematic sketch of the plate tectonic situation in the Pacific Basin during the Late Cretaceous to Eocene period as indicated by magnetic anomalies preserved on the Pacific plate [after *Doubrovine and Tarduno*, 2008]. Resurrection plate after *Haeussler et al.* [2003]. Two possible locations of the accretionary prism of the Chugach and Prince William terranes along the margin are indicated. Abbreviations of geographical locations (in italics) are as follows: Anc, Anchorage; Ba, Baranof Island; Co, Cordova; GI, Glacier Island; Ju, Juneau; KI, Knight Island; Ko, Kodiak; MtF, Mount Fairweather; Se, Seward; SeG, Seward Glacier; RP, Resurrection Peninsula; Si, Sitka; Va, Valdez; Ya, Yakutat. Abbreviations of geological names (terrane names in boxes and bold font; faults in bold font) are as follows: ARB, Alaska Range belt; BRFS, Border Range Fault System; CFS, Contact Fault System; CMC, Chugach Metamorphic Complex; CSE, Chugach–St. Elias Fault; CSF, Chatham Strait Fault; CT, Chugach terrane; CPC, Coast Plutonic Complex; DF, Denali Fault; DRZ, Dangerous River Zone; FF, Fairweather Fault; KF, Kaltag Fault; KIZ, Kayak Island Zone; PZ, Pamplona Zone; PWT, Prince William terrane; TF, Tintina Fault; TrF, Transition Fault; WCT, Wrangellia Composite terrane; YT, Yakutat terrane.

accretionary prism of the Chugach terrane [e.g., *Hudson and Plafker*, 1982; *Sisson et al.*, 1989; *Plafker et al.*, 1994]. The structural evolution of its northern and western part is relatively well known [*Sisson and Pavlis*, 1993; *Pavlis and Sisson*, 1995, 2003], and its metamorphic history is controlled by low- to medium-pressure/high-temperature metamorphism [*Sisson et al.*, 1989; *Bruand*, 2011]. In the following, we present (1) the results of structural field work along three across-strike composite sections across the complex (Figure 2), therewith extending the structural studies of *Pavlis and Sisson* [1995,

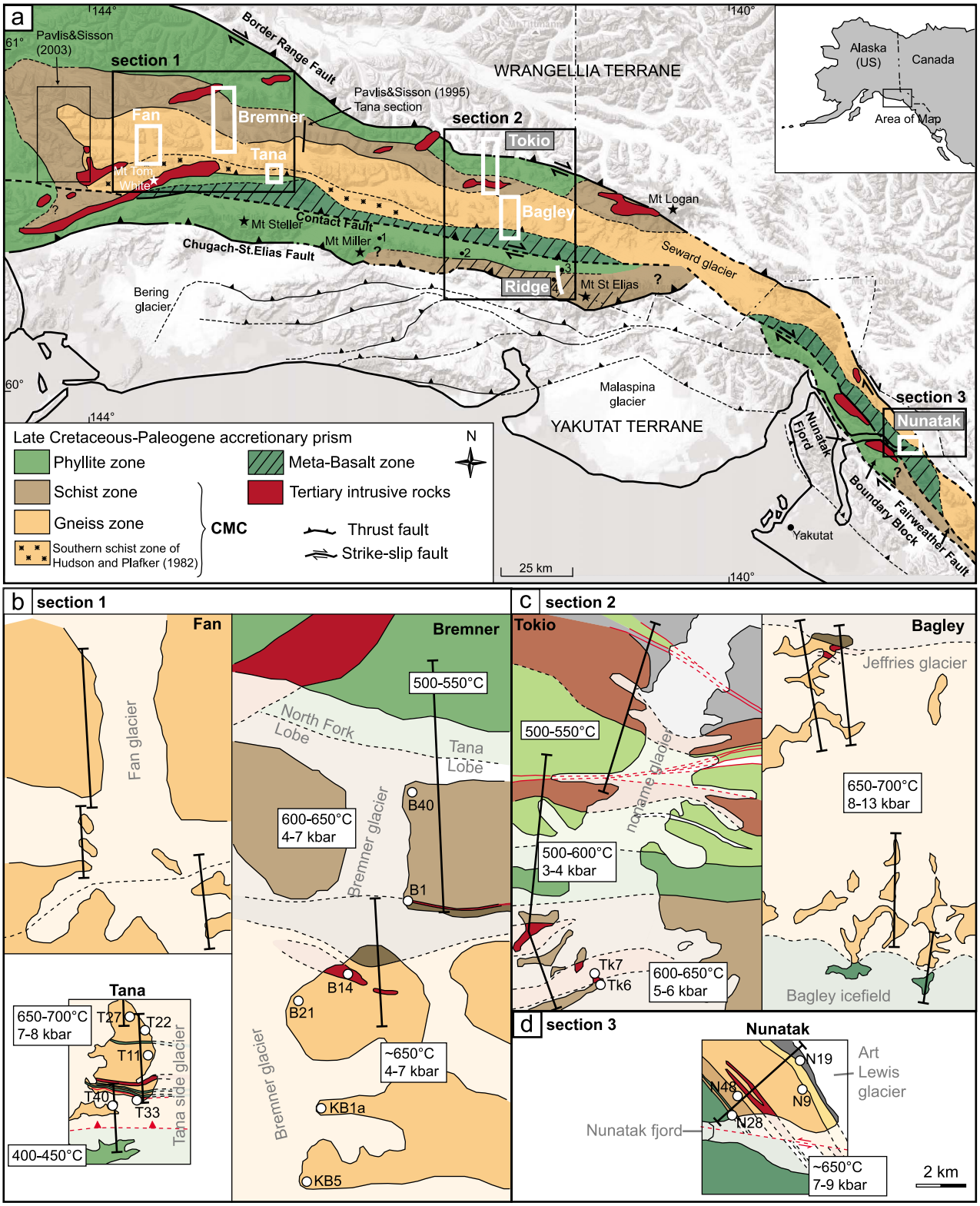

Figure 2

2003] toward the south and east, and (2) the results of $^{40}Ar/^{39}Ar$, Rb-Sr and zircon fission track thermochronology conducted on the three structural transects investigated. Based on these new thermochronological data and data from the literature, we present cooling paths for the different parts of the complex. We then integrate the structural, metamorphic and temporal history to present a possible tectonic evolution for the complex. Our study documents the structural, metamorphic and temporal behavior of middle to lower crust along an obliquely convergent continental margin from ~60 Ma to the present.

2. Geological Setting

[4] The CMC is exposed in the Chugach–St. Elias Mountains along the southern Alaskan margin (Figure 1). The southern Alaskan margin is part of the outermost tectonic belt of the North American Cordillera (Figure 1a [*Oldow et al.*, 1989; *Dickinson*, 2009]), which resulted from the (ongoing) oblique convergence between oceanic plates of the Pacific Basin and the continent of North America. The modern margin is highly curved, which leads to dominantly dextral movement along the active Fairweather fault system in southeastern Alaska and to thrust faulting along the Aleutian megathrust and related faults farther west (Figure 1b). A block of continental and oceanic crust, the Yakutat terrane, is currently actively colliding into this curved margin (Figure 1b [e.g., *Bruhn et al.*, 2004; *Pavlis et al.*, 2004; *Berger et al.*, 2008; *Meigs et al.*, 2008]).

[5] The rocks located inboard of the Yakutat terrane are part of a vast, complexly deformed accretionary prism which extends ~2100 km along the margin from Sanak Island in the west to Baranof Island in the southeast (Figure 1b; Chugach and Prince William terranes). This accretionary prism is emplaced along the Border Range fault system against the Wrangellia composite terrane to the north (Figure 1b [*Plafker et al.*, 1994; *Pavlis and Roeske*, 2007]). The accretionary prism is built of (1) an inboard narrow belt of Late Triassic to Cretaceous mélange [e.g., *Amato and Pavlis*, 2010] and (2) an outboard Late Cretaceous to Eocene marine turbidite sequence intercalated with mafic volcanic rocks (Figure 1b [*Nilsen and Zuffa*, 1982; *Plafker et al.*, 1994]). The accretionary prism is separated into the northern Chugach and the southern Prince William terranes by the Contact fault system (Figure 1b [*Bol and Gibbons*, 1992; *Bol and Roeske*, 1993]).

[6] Paleocene to Eocene magmatic rocks intrude the accretionary prism of the Chugach and the northern part of the Prince William terrane: the so-called Sanak-Baranof plutonic belt (Figure 1b [*Hudson et al.*, 1979; *Farris and Paterson*, 2009]). The mainly calc-alkaline plutons are unusual because they intrude the accretionary prism in an extreme fore-arc position: inferred coeval magmatic arcs are located a few hundred kilometers farther inboard (the Alaska Range and Coast Plutonic belts; Figure 1a [*Wallace and Engebretson*, 1984; *Plafker et al.*, 1994]). The geochemistry of the Sanak-Baranof plutons indicates that they originated mainly from the melting of metasedimentary rocks of the accretionary prism, with a variable contribution from a more mafic end-member [*Hudson et al.*, 1979; *Hill et al.*, 1981; *Barker et al.*, 1992; *Harris et al.*, 1996; *Lytwyn et al.*, 2000; *Ayuso et al.*, 2009]. The age of the intrusions ranges from ~61 Ma in the west to ~50 Ma in the east [*Bradley et al.*, 1993, 2000, 2003; *Sisson et al.*, 2003; *Farris et al.*, 2006].

[7] The CMC is exposed in the eastern part of the accretionary prism and is intruded by many premetamorphic, synmetamorphic and postmetamorphic dikes and plutons associated with the Sanak-Baranof belt (Figures 1b and 2a [*Hudson and Plafker*, 1982; *Sisson and Pavlis*, 1993; *Pavlis and Sisson*, 1995, 2003; *Harris et al.*, 1996]). The complex consists of two macroscopically different metamorphic units: An outer schist zone composed of fine-grained biotite-quartz-plagioclase schist, which surrounds an inner gneiss zone composed of layered migmatitic gneisses (Figure 2a [*Hudson and Plafker*, 1982]). A zone of metabasaltic rocks intercalated with greenschist- to amphibolite facies metasedimentary rocks occurs along the southern border of the complex (Figure 2a [*Lull and Plafker*, 1990]). Peak metamorphic conditions reached are ~450°C–550°C and ~2–3 kbar in the greenschist-facies phyllites outside the CMC, ~500°C–650°C and ~2–3 kbar in the northern schist zone and in the westernmost gneiss zone, ~500°C–650°C and ~3–7 kbar in the southern schist zone, and >650°C and ~4–13 kbar in the gneiss zone, with a tendency of the higher pressures occurring toward the south and east (Figures 2b–2d [*Sisson and Hollister*, 1988; *Sisson et al.*, 1989; *Bruand et al.*, 2010; *Bruand*, 2011]). Based on these pressure ranges, rocks of the phyllite, schist, western and northern gneiss zones apparently reached maximum depths of ~10–25 km whereas rocks of the southern and eastern gneiss zones were buried to depths of up to ~30–50 km.

[8] Structurally, the northern schist zone and the western gneiss zone of the CMC are dominated by three generations of ductile fabrics [*Sisson and Pavlis*, 1993; *Pavlis and Sisson*, 1995, 2003; *Scharman et al.*, 2011].

[9] 1. D_1 produced a variably but generally steeply dipping layer-parallel pressure solution foliation (S_1). In line with observations in lower-grade rocks to the west [e.g., *Nokleberg*

Figure 2. (a) Geological map of the Chugach Metamorphic Complex, according to *Hudson and Plafker* [1982] and results of this study. The locations of the three different sections presented in this study are indicated. Note that *Hudson and Plafker* [1982] mapped a southern schist zone in the western part of the complex (indicated with stars) which we did not encounter in our sections 1 and 2. Dots labeled 1–4 in the southern phyllite zone are locations of fixed-wing aircraft stops we conducted in order to map the structure of the ridge between Mount Miller and Mount St. Elias. (b–d) Detailed sketch maps of the different parts of the western, central, and southeastern sections. The location of the thermochronological samples and general *PT* conditions from *Bruand* [2011] are indicated. The given *PT* ranges in boxes correspond to the *PT* ranges obtained on several samples from these zones, including error bars on the methods used. Scale bar in Figure 2d applies to all sections in Figures 2b–2d. Stippled line in the Fan transect of Figure 2b indicates the southern gneiss-schist transition as marked on the map of *Hudson and Plafker* [1982]. Color code as for Figure 3 for Figures 2b and 2c and as for Figure 4 for Figure 2d.

et al., 1989; *Fisher and Byrne*, 1992] this deformational event is generally interpreted as contemporaneous with accretion.

[10] 2. D_2 produced the first syn-CMC metamorphic fabric (S_2) with a pronounced E-W stretching lineation developed in the schists and gneisses, associated with gently inclined to recumbent, close to isoclinal F_2 folds.

[11] 3. D_3 produced a steeply dipping, ~E-W striking foliation (S_3) developed as a crenulation cleavage in the schist zone and as a high-grade foliation contemporaneous with migmatite development in the gneiss zone. D_3 was associated with dextral shear, with localized evidence that D_3 was transpressional.

[12] The CMC is less well known to the east and south of the U.S.-Canadian border. From the core of the St. Elias Mountains through the Fairweather Range, the CMC is extensively covered by ice fields (Figure 2a), but the high-grade metamorphism probably extends continuously to at least the Fairweather Range (Figure 1b) and may extend as far as Baranof Island [e.g., *Pavlis and Sisson*, 1995; *Zumsteg et al.*, 2003; *Bruand*, 2011]. Complications occur along the southern border of the CMC [e.g., *Plafker et al.*, 1994]. Tectonic slivers of accretionary prism rocks with variable metamorphic grade (e.g., the ridge from Mount Steller to Mount St. Elias and the Boundary block in the Nunatak Fjord area; Figure 2a) were probably dextrally displaced and obliquely exhumed along the Fairweather-Contact fault system, but little is known about the timing and amount of displacement and exhumation [*Hudson et al.*, 1977a, 1977b; *Plafker et al.*, 1994; *Sisson et al.*, 2003; *Enkelmann et al.*, 2009, 2010].

[13] The presence of the high-grade CMC in the accretionary prism, the near-trench position of the Sanak-Baranof plutonic belt and the geochemistry and age distribution of these plutons have been widely interpreted as the result of the subduction of an active oceanic spreading ridge below the margin, with the subducting ridge providing the heat for metamorphosing and melting the accreted sedimentary rocks [*Marshak and Karig*, 1977; *Bradley et al.*, 1993, 2000, 2003; *Sisson and Pavlis*, 1993; *Pavlis and Sisson*, 1995, 2003; *Haeussler et al.*, 1995, 2003; *Harris et al.*, 1996; *Madsen et al.*, 2006; *Farris and Paterson*, 2009]. However, due to unknown dextral displacement of the accretionary prism along the Border Range fault system since its formation (Figure 1d [e.g., *Plafker et al.*, 1994; *Roeske et al.*, 2003; *Pavlis and Roeske*, 2007]) and the incomplete plate tectonic record in the Pacific basin (Figure 1d [e.g., *Engebretson et al.*, 1985; *Atwater*, 1989; *Doubrovine and Tarduno*, 2008]), different plate tectonic models have been proposed which could explain the Eocene tectonic history of the southern Alaskan margin (Figure 1d [*Bradley et al.*, 1993, 2003; *Sisson and Pavlis*, 1993; *Pavlis and Sisson*, 1995; *Haeussler et al.*, 2003; *Madsen et al.*, 2006]).

3. New Structural Data From the Chugach Metamorphic Complex

[14] In order to extend the structural information from *Pavlis and Sisson* [1995, 2003] from the northern and western parts of the CMC to a larger area, we mapped three across-strike composite sections through the entire complex (Figure 2): (1) a western section 1, (2) a central section 2, and (3) a southeastern section 3. Access to the sections was by fixed wing aircraft and mapping occurred on foot from central camps. A total of 45 field days were conducted over two summers (2008, 2009). In the following, we refer to the schist and gneiss zones as macroscopically defined by *Hudson and Plafker* [1982] and we refer to the lower-grade metamorphic rocks outside the complex as phyllite zone.

[15] Section 1 consists of three different field areas: the Fan, Bremner and Tana transects (named after the major glaciers close to the transects; Figures 2a, 2b, and 3a). The section crosses from the phyllite to the gneiss zone in the north (Bremner transect), traverses the gneiss zone (Fan transect) and crosses from the gneiss zone to the phyllite zone in the south (Tana transect; Figure 3a). Section 2 lies ~70–90 km east of section 1 and covers the central part of the CMC (Figures 2a, 2c, and 3b). The section runs from the Wrangellia terrane in the north into the schist zone of the CMC (Tokio transect) and across the gneiss zone into the southern metabasalt zone (Bagley transect). In addition, we conducted four fixed wing aircraft stops along the highly glaciated ridge between Mount Miller and Mount St. Elias (stops 1–4; Figure 2a) and we draw a profile across this ridge in the Mount Huxley region (Figures 2a and 3b). Section 3 lies ~170 km southeast along strike of section 2 (Figures 2a, 2d, and 4). The section is the first relatively easily accessible transect across the CMC southeast of the high-alpine St. Elias range. The Chugach terrane in section 3 is limited to a narrow strip ~10 km in width between the Border Range fault system in the northeast and the Fairweather fault system in the southwest (Figures 2a and 4). In addition to this decrease in total width, the strike of the Chugach terrane changes from ~W-E in sections 1 and 2 to NW-SE in section 3. Two different lithological units comprise the Chugach terrane in section 3 (Figure 4): a northeastern, ~4–5 km wide unit of variable gneisses and altered schists and a southwestern, ~4–5 km wide unit of fine-grained amphibolites that are interpreted as metabasalts (Figures 2a and 4).

[16] Detailed structural descriptions of each section can be found in Text S1, and field photographs of each section can be found in Figures S1–S3.[1] A summary of our structural observations is presented in Figure 5 as a tectonic sequence diagram [after *Forster and Lister*, 2008] where the different observations from each transect are correlated (1) with each other, (2) with the mineral growth events observed in the rocks [*Bruand*, 2011] and (3) with the deformational sequence observed by *Pavlis and Sisson* [1995, 2003] in the western and northern part of the complex (Figure 2a). A schematic 3-D sketch of the complex is displayed in Figure 6. Our results together with the observations of *Pavlis and Sisson* [1995, 2003] and the petrological evolution as described by *Bruand* [2011] reveal the following structural and metamorphic evolution in the CMC.

3.1. First Deformational Phase

[17] In the phyllite zone of sections 1 and 2 and the northern schist zone of section 2, tight to isoclinal folds with E-W trending fold axes are present, accompanied by an axial planar pressure solution foliation (Figures S1a and S2b and Figure 5, correlated with D_1 after *Pavlis and Sisson*

[1] Auxiliary material data sets are available at ftp://ftp.agu.org/apend/tc/2010tc002776. Other auxiliary material files are in the HTML.

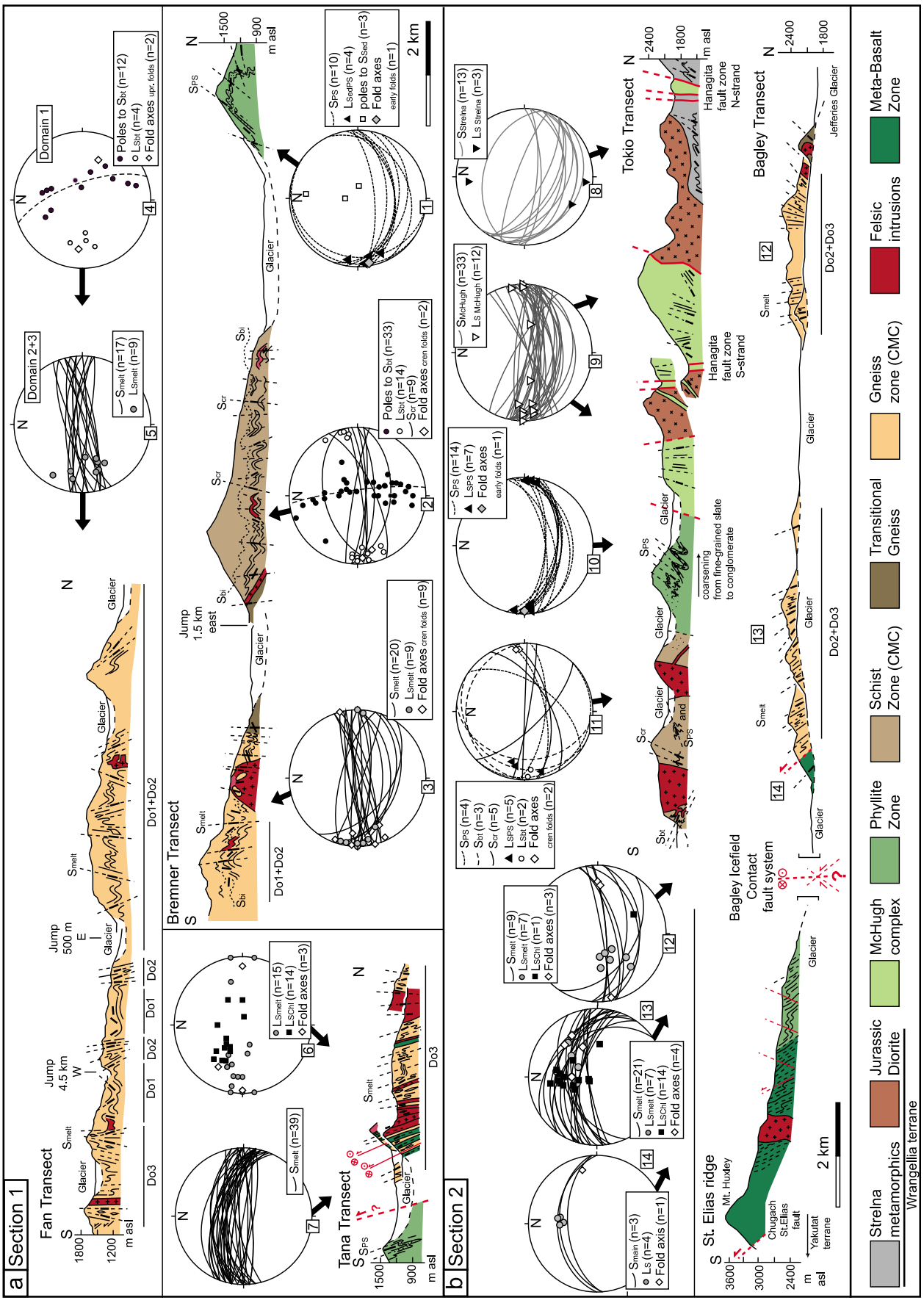
a Section 1
Fan Transect
Jump 4.5 km W
Jump 500 m E
Glacier
Do3
Do1
Do2
Do1+Do2
m asl
Domain 1
Domain 2+3
Poles to Sbt (n=12)
LSbt (n=4)
Fold axes upr. folds (n=2)
Smelt (n=17)
LSmelt (n=9)
Bremner Transect
Jump 1:5 km east
SPS
Sbi
Scr
Smelt
Glacier
2 km
Poles to Sbt (n=33)
LSbt (n=14)
Scr (n=9)
Fold axes cren folds (n=2)
Smelt (n=20)
LSmelt (n=9)
Fold axes cren folds (n=9)
SPS (n=10)
LSedPS (n=4)
poles to SSed (n=3)
Fold axes early folds (n=1)
Tana Transect
Smelt (n=39)
LSmelt (n=15)
LSChl (n=14)
Fold axes (n=3)
Do3
b Section 2
SPS (n=4)
Sbt (n=3)
Scr (n=5)
LSPS (n=5)
LSbt (n=2)
Fold axes cren folds (n=2)
SPS (n=14)
LSPS (n=7)
Fold axes early folds (n=1)
SMcHugh (n=33)
LS McHugh (n=12)
SStrelna (n=13)
LS Strelna (n=3)
Smelt (n=9)
LSmelt (n=7)
LSChl (n=1)
Fold axes (n=3)
Smain (n=3)
LS (n=4)
Fold axis (n=1)
Smelt (n=21)
LSmelt (n=7)
LSChl (n=14)
Fold axes (n=4)
Tokio Transect
Hanagita fault zone S-strand
Hanagita fault zone N-strand
coarsening from fine-grained slate to conglomerate
Bagley Transect
Do2+Do3
Jefferies Glacier
St. Elias ridge
Mt. Huxley
Chugach St.Elias fault
Yakutat terrane
Bagley Icefield Contact fault system
Strelna metamorphics
Wrangellia terrane
Jurassic Diorite
McHugh complex
Phyllite Zone
Schist Zone (CMC)
Transitional Gneiss
Gneiss zone (CMC)
Felsic intrusions
Meta-Basalt Zone

Figure 3

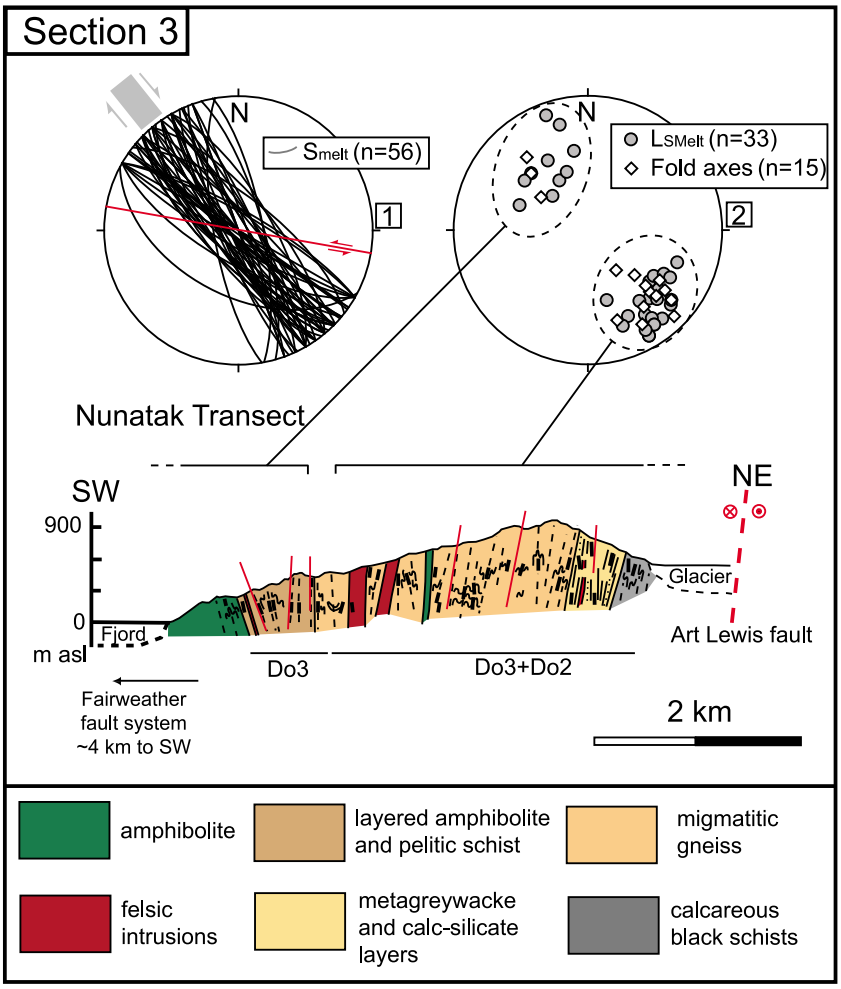

Figure 4. Structural profile and stereoplots from section 3 of the CMC. Stereoplots are lower hemisphere equal area projections, computed with StereoNett software version 2.46 of Johannes Duyster.

[1995, 2003]). Since this fabric is the first which developed in the metasedimentary rocks, it is probably related to the accretion of the sediments. However, it is interesting to note that in sections 1 and 2, these early folds are asymmetric to the north, and the corresponding axial planar foliation is south dipping, contrary to D_1 structures related to accretion described farther west in the area of Prince William Sound which are generally north dipping and asymmetric to the south [e.g., *Plafker et al.*, 1994]. Biotite is present in the northern phyllite zone of section 1, whereas only chlorite is present in the southern phyllite zone of section 1 and the entire phyllite zone of section 2. Peak metamorphic conditions reached during that stage in the phyllites are ~500°C–550°C and ~2–3 kbar in the north and ~400°C–450°C in the south (Figures 2b and 2c [*Sisson et al.*, 1989; *Bruand*, 2011]).

3.2. Second Deformational Phase

[18] In the entire schist zone of section 1, in the southern schist zone of section 2 and in the entire gneiss zone of all sections, an originally flat-lying penetrative foliation defined by biotite ± sillimanite is developed, which dips below the D_1 fabric domain in the northern schist zone and the phyllites of sections 1 and 2 (Figures S1b, S1c, and S2c

Figure 3. (a) Structural profiles across the western CMC separated into three parts from north to south: the Bremner, Fan, and Tana transects. (b) Structural profiles across the central CMC separated into three parts from north to south: the Tokio, Bagley and St. Elias ridge transects. Stereoplots are lower hemisphere equal area projections, computed with StereoNett software version 2.46 of Johannes Duyster. The stereoplots are numbered from 1 to 14 (SP1–SP14; referenced in the text). Abbreviations are as follows: SP, Stereoplot; and, andalusite; S_{PS}, pressure solution foliation; L_{SedPS}, intersection lineation between bedding and pressure solution foliation; L_{SPS}, stretching lineation on pressure solution foliation; S_{Sed}, sedimentary bedding; S_{bt}, foliation defined mainly by biotite; L_{Sbt}, stretching lineation defined by biotite; S_{cr}, crenulation foliation; S_{melt}, foliation defined mainly by leucosomes and partly biotite; L_{Smelt}, stretching lineation on S_{melt}; L_{SChl}, late stretching lineation defined by chlorite. Do1, low D_3 strain intensity; Do2, intermediate D_3 strain intensity; Do3, high D_3 strain intensity. See detailed descriptions in Text S1.

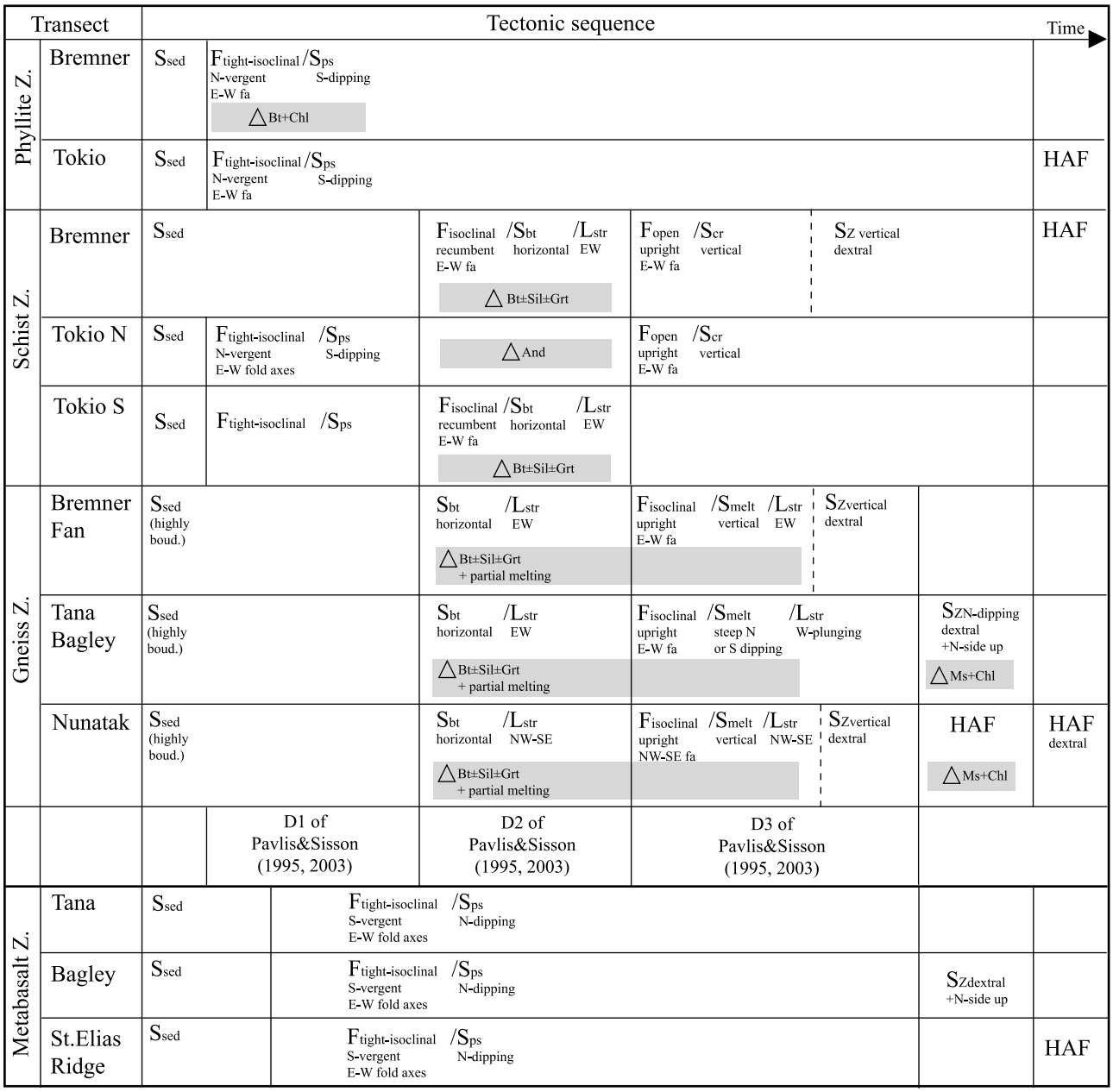

Figure 5. Tectonic sequence diagram for the Chugach Metamorphic Complex drawn according to the method described by *Forster and Lister* [2008]. The different fabrics observed in each zone on each transect are correlated with each other, with the mineral growth events observed in the rocks and with the structural scheme described by *Pavlis and Sisson* [1995, 2003]. F denotes observed folding phase, with the corresponding geometrical description in subscript (shape of folds, fold vergence, orientation of fold axes (fa)). S denotes observed planar fabric, with the following subscripts: sed, sedimentary bedding; PS, pressure solution; bt, defined by biotite; cr, crenulation; melt, defined by leucosomes. In addition, the orientation of the planar fabric is given (horizontal versus vertical). L denotes observed lineation, with str, stretching lineation and the orientation of the lineation indicated. SZ denotes observed shear zone, with orientation and shear sense indicated. HAF denotes high-angle (close to vertical) brittle faults. Slashes between fabric elements indicate that they probably formed simultaneously. Gray bars indicate mineral growth and partial melting events relative to the fabric development.

and Figure 5, correlated with D_2 after *Pavlis and Sisson* [1995, 2003]). This fabric is axial planar to isoclinal folds with E-W fold axes, which are parallel to a pronounced E-W subhorizontal stretching lineation. Finite strain analyses of *Pavlis and Sisson* [1995, 2003] indicate that this D_2 fabric records margin-parallel stretching accompanied by vertical flattening which affected the lower part of the accretionary prism. Besides this well defined pure shear component the

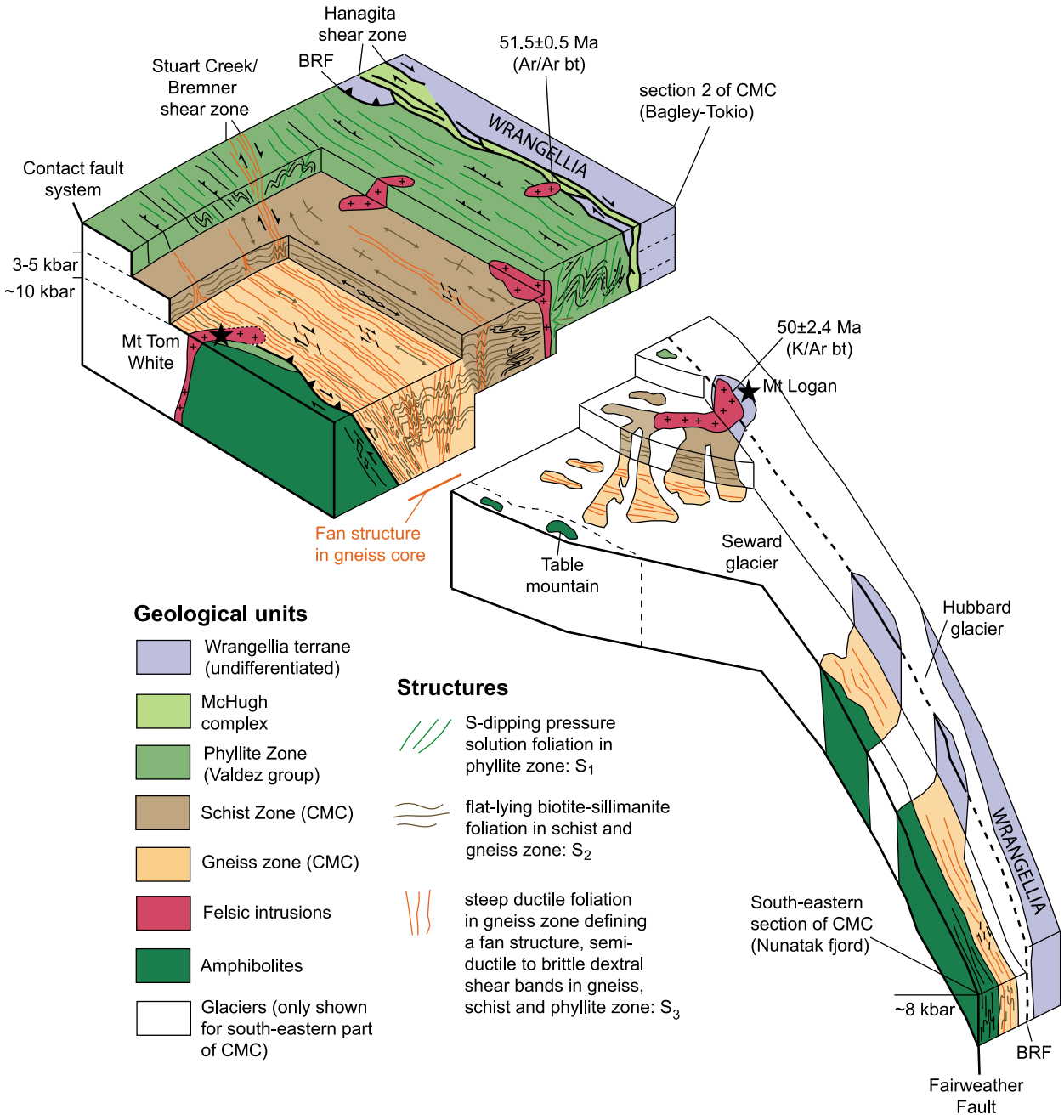

Figure 6. Schematic 3-D sketch of the Chugach Metamorphic Complex with the dominant fabrics indicated. The CMC has a pronounced asymmetric shape with a wide transition from phyllite to gneiss in the north and an abrupt juxtaposition of gneiss against phyllites and metabasalts in the south. Two K/Ar biotite ages from two plutons intruding the Border Range Fault System to the north of the complex are given [from *Roeske et al.*, 2003; *Bradley et al.*, 1993] which indicate that fault activity along these particular fault strands must have occurred before ~52–50 Ma.

amount of simple shear involved in the formation of the D_2 fabric is not well constrained. Sparse observations of top-to-the-east shear sense perpendicular to the S_2 planes and parallel to the E-W lineation [*Pavlis and Sisson*, 1995, 2003] (also this study) may point to an unknown amount of simple shear deformation during the D_2 deformation. The D_2 fabric development is clearly contemporaneous with biotite, sillimanite and garnet growth in the schist zone and with the onset of partial melting in the gneiss zone. The andalusite crystals observed in the northern schist zone of section 2 occur structurally just above the D_2 fabric front and we interpret this andalusite growth as contemporaneous with the bt ± sil ± grt growth in the D_2 fabric domain structurally below (Figure 5). Peak metamorphic conditions were reached in the schist zone contemporaneous with D_2 and are ~600°C–650°C and ~5–7 kbar (Figures 2b and 2c [*Bruand*, 2011]).

3.3. Third Deformational Phase

[19] Both the schist and the gneiss zones in all three sections are overprinted by variably open to isoclinal upright folds with steeply dipping axial planes and E-W fold axes (Figures S1d, S1e, and S1f and Figure 5, correlated with D_3 after *Pavlis and Sisson* [1995, 2003]). In the schist zone, a steeply dipping, spaced crenulation cleavage is developed axial planar to the folds and often steep brittle fault zones are developed in the core of these folds. In the schist zone, the D_3 deformation probably set in at or shortly after the metamorphic peak (Figure 5). In the gneiss zone, the D_3 deformation is developed strongly domainal, with domains of low, intermediate and high D_3 strain (domains 1–3; Figure 3). In the intermediate and high D_3 strain domains, a new axial planar foliation to the upright folds is developed, defined by biotite, sillimanite and leucosome layers, indicating that partial melting and metamorphic mineral growth was ongoing during D_3 in the gneiss zone. This newly formed steep foliation defines a large-scale foliation fan in the entire gneiss zone (Figure 6). In the northern gneiss zone the ductile stretching lineation associated with this D_3 fabric is oriented subhorizontal and E-W, whereas in the southern gneiss zone the ductile stretching lineation on the D_3 foliation is plunging steeply to the west-northwest (Figure 3). Finite strain measurements of *Pavlis and Sisson* [1995, 2003] revealed a horizontal shortening component during D_3 fabric formation. Dextral shear bands, which developed simultaneous to and overprinting the D_3 foliation, point to an important dextral component of simple shear during the D_3 deformation, indicating that D_3 was a dextral transpressive event (Figure 5). The gneiss zone probably reached its metamorphic peak mainly during this D_3 deformation, with peak temperatures of ~650°C–700°C in all sections and peak pressures of 4–8 kbar in section 1, ~8–13 kbar in section 2 and 7–9 kbar in section 3 (Figures 2b–2d [*Bruand*, 2011]).

3.4. Postmetamorphic Shear Zones and Brittle Faults in the South of the Complex

[20] The southern border of the CMC west of the U.S. Canadian Border is made up of a series of ductile to brittle postmetamorphic fault zones which juxtapose high-grade gneisses in the north against low-grade phyllites in the south (Figures 2a and 3). The southern schist zone as proposed by *Hudson and Plafker* [1982] between the gneisses and the phyllites does not exist and probably has been cut out by these faults and shear zones. Muscovite- and chlorite-coated stretching lineations in these shear zones plunge to the west-northwest and shear sense indicators reveal north-side-up and dextral sense of movement along these faults (Figure 3). The presence of these shear zones and faults in the south of the complex, together with the concentration of high D_3 strain domains with down-dip lineations along the southern border produce a highly asymmetric final shape of the complex, with a wide transition from phyllites to gneisses in the north and an abrupt juxtaposition of gneisses against lower-grade phyllites in the south (Figure 6).

4. Thermochronology

[21] Peak metamorphic conditions reported for the CMC are ~600°C–650°C at depths of ~10–20 km in the northern schist zone and ~600°C–700°C at depths of ~20–50 km in the southern and eastern gneiss zone of the complex (Figure 2 [*Sisson et al.*, 1989; *Bruand*, 2011]). The timing of these peak metamorphic conditions is revealed by U-Pb dating of metamorphic zircon overgrowths in the gneisses to ~55–51 Ma all over the complex (Table 1 [*Gasser*, 2010]). In contrast to the homogenous age of the peak metamorphic conditions, existing thermochronological data point to variations in the timing of cooling and exhumation along and across strike of the complex, with considerably younger ages toward the southeast [*Hudson et al.*, 1977a, 1977b; *Onstott et al.*, 1989; *Sisson et al.*, 1989; *Sisson et al.*, 2003; *Berger et al.*, 2008; *Enkelmann et al.*, 2008, 2010]. In order to constrain the timing of cooling and exhumation in more detail, we present in the following (1) a compilation of existing thermochronological data for the CMC, (2) new $^{40}Ar/^{39}Ar$, Rb/Sr and fission track ages and (3) an interpretation of these ages in terms of cooling curves for sections 1–3 of the metamorphic complex.

4.1. Summary of Previous Thermochronological Data

[22] A compilation of published $^{40}Ar/^{39}Ar$ and low-temperature geochronology data for the three sections of the CMC is displayed in Figure 7. Since the data come from throughout the CMC, we extended our definitions of sections 1–3 to include larger areas (Figure 7). The compilation includes five $^{40}Ar/^{39}Ar$ ages on hornblende, biotite and plagioclase (Figure 7 [*Sisson et al.*, 1989, 2003]). A large dataset of detrital zircon fission track ages of modern river sands draining the western and central part of the CMC show a maximum at ~20–35 Ma [*Enkelmann et al.*, 2008, 2010], which corresponds well with two zircon fission track ages from bedrock samples from section 2 [*Meigs et al.*, 2008] (Figure 7). One bedrock zircon fission track age is available for section 3, which is considerably younger than the ages from sections 1 and 2 (Figure 7 [*McAleer et al.*, 2009]). River sand draining the Seward glacier area shows a very young fission track signal (<3 Ma, with some ages <1 Ma [*Enkelmann et al.*, 2009]). In addition, four (U-Th)/He zircon ages, 12 apatite fission track ages and 19 (U-Th)/He apatite ages are available in the literature (Figure 7 [*O'Sullivan et al.*, 1997; *Spotila et al.*, 2004; *Berger and Spotila*, 2008; *Berger et al.*, 2008; *McAleer et al.*, 2009; *Enkelmann et al.*, 2010]).

4.2. New Thermochronological Data

4.2.1. The $^{40}Ar/^{39}Ar$ Dating of Muscovite and Biotite

[23] Seven muscovite-bearing samples and 12 biotite-bearing samples were selected for $^{40}Ar/^{39}Ar$ furnace step heating analyses. The sample locations are displayed in Figures 2 and 7. Sample coordinates, rock type, mineralogy, *PT* conditions and $^{40}Ar/^{39}Ar$ ages are summarized in Table 1. Three of the seven muscovite samples come from undeformed igneous rocks (B1, B14 and B19). B1 is derived from an up to ~5 m thick felsic dike intruding the schist zone in the Bremner transect (Figure 2). This dike is oriented parallel to S_{bt}, but is internally not deformed. B14 is from a several 100 meters wide felsic intrusion in the northern gneiss zone of the Bremner transect (Figure 2). B19 is from a ~20 cm wide cross-cutting pegmatitic dike exposed in the Nunatak transect (Figure 2). In all three igneous samples, coarse muscovite occurs randomly oriented

Table 1. Summary of All Samples Used for Geochronology

Number	Transect	Latitude (°N)	Longitude (°W)	Rock Type	Mineralogy[a]	*PT* Conditions[b]	U/Pb Zrn[c] (Ma) ±2σ	$^{40}Ar/^{39}Ar$ Ms (Ma) ±2σ	$^{40}Ar/^{39}Ar$ Bt (Ma) ±2σ	Rb-Sr Bt, WR (Ma) ±2σ	FT Zrn (Ma) ±2σ
91Asn11[d]		60.8236	144.2500	gneiss	Grt	650°C ± 30°C[e]	52.8 ± 1.0				30.9 ± 8.6
B40	Bremner	60.8883	143.2384	schist	Grt-Sil-Ms	*597°C ± 50°C*[f]			47.6[g] ± 2.3	50.3 ± 0.5	
B21	Bremner	60.8124	143.3148	gneiss	Ms	-			48.4 ± 2.1		28.1 ± 2.8
KB1	Bremner	60.7643	143.2881	gneiss	Ms-Grt-Sil	*666°C ± 30°C*[e], 5.1 ± 1.6 kbar[h]			50.0 ± 2.2	49.9 ± 0.5	
KB5	Bremner	60.7381	143.3015	gneiss	Ms	>640°C[f]	54.0 ± 0.8		47.3 ± 2.1	48.6 ± 0.5	
B1	Bremner	60.8496	143.2388	dike	Qz-Plag-Ms	-		45.8 ± 2.1			
B14	Bremner	60.8233	143.2777	intrusion	Qz-Plag-Ms	-		53.4 ± 2.9			
T27	Tana	60.7146	142.9147	gneiss	Ms-Grt	680°C ± 30°C/7.3 ± 1.1 kbar[h], 710°C–720°C/8–9 kbar[i]	52.6 ± 0.8		49.2[g] ± 2.5		
T22	Tana	60.7108	142.9036	gneiss	Ms	-		46.2 ± 2.3	47.3 ± 2.0		
T11	Tana	60.7013	142.9004	gneiss	Ms-Grt	-			47.5[g] ± 2.3	49.4 ± 0.5	
T33	Tana	60.6856	142.9034	fault rock	Ms-Sil	*679°C ± 30°C*[e]			46.9 ± 2.1		
T40	Tana	60.6828	142.9238	gneiss	Ms	>640°C[f]	54.0 ± 0.9		47.0 ± 2.0	48.5 ± 0.5	28.9 ± 2.4
Tk6	Tokio	60.6642	141.5488	schist	Sil(And)-Ms	*658°C ± 33°C/6.4 ± 1.4 kbar*[h], 655°C ± 30°C[e]		49.0[g] ± 2.8			
Tk7	Tokio	60.6671	141.5521	intrusion	Ms	-	54.0 ± 0.8		49.1[g] ± 2.8		
Loc4	Bagley	60.5544	141.3030	gneiss	Grt-Sil-Ms	666°C ± 25°C/8.2 ± 1.2 kbar[h], 674°C ± 30°C[e]	53.0 ± 0.7		47.4 ± 2.1	48.9 ± 0.5	26.0 ± 2.8
N9	Nunatak	59.8223	138.8313	gneiss	Ms	*>640°C*[f]	51.3 ± 0.7	22.6[g] ± 1.1	15.8 ± 0.8	14.9 ± 0.2	
N28	Nunatak	59.8151	138.8827	mylonite	Ms-Grt-Sil	*644°C ± 29°C/8.2 ± 1.0 kbar*[h], ~680°C/~10 kbar[i]		20.0 ± 1.0			
N48	Nunatak	59.8210	138.8783	gneiss	Ms-Grt-Sil	-				14.9 ± 0.2	
N19	Nunatak	59.8330	138.8314	pegmatite	Qz-Plag-Ms	-		36.2[g] ± 2.2			

[a]Mineral abbreviations after *Whitney and Evans* [2010]. Italic values represent that PT information is not from sample itself but from other sample from the same outcrop.
[b]PT conditions are from *Bruand* [2011].
[c]U-Pb zircon ages are from *Gasser* [2010].
[d]Sample courtesy of V. B. Sisson.
[e]Biotite-Garnet thermometry.
[f]Graphite thermometry.
[g]Error plateau age (see text).
[h]AverageP(T) calculation (Thermocalc).
[i]Pseudosection estimate (Thermocalc).

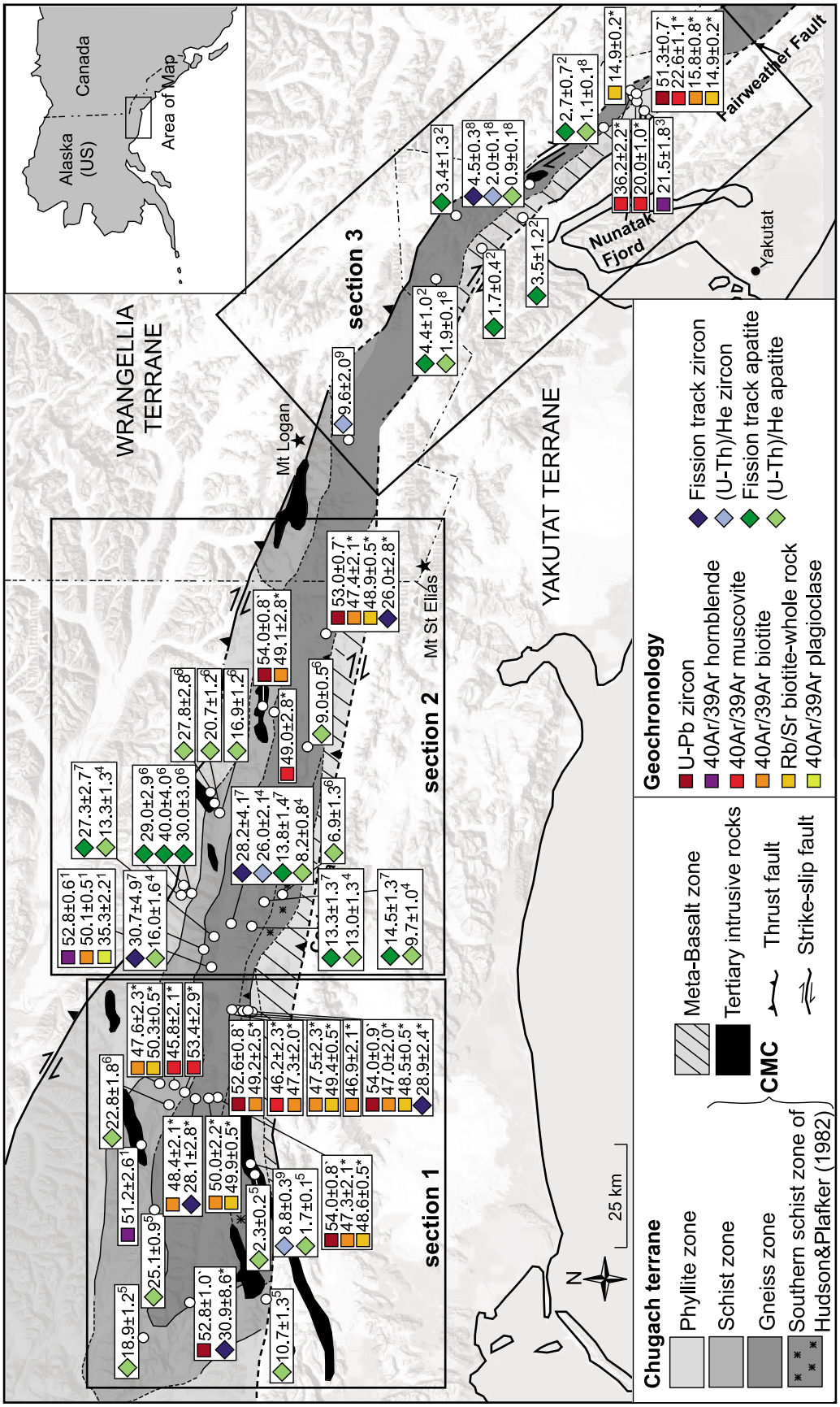

Figure 7. Compilation of geochronological data for the CMC. References are as follows: 1, *Sisson et al.* [1989]; 2, *O'Sullivan et al.* [1997]; 3, *Sisson et al.* [2003]; 4, *Spotila et al.* [2004]; 5, *Berger and Spotila* [2008]; 6, *Berger et al.* [2008]; 7, *Meigs et al.* [2008]; 8, *McAleer et al.* [2009]; 9, *Enkelmann et al.* [2010]; grave accent, *Gasser* [2010]; asterisk, this study (Table 1 and Figure 2). Note that the definitions of sections 1–3 are enlarged compared to Figure 2.

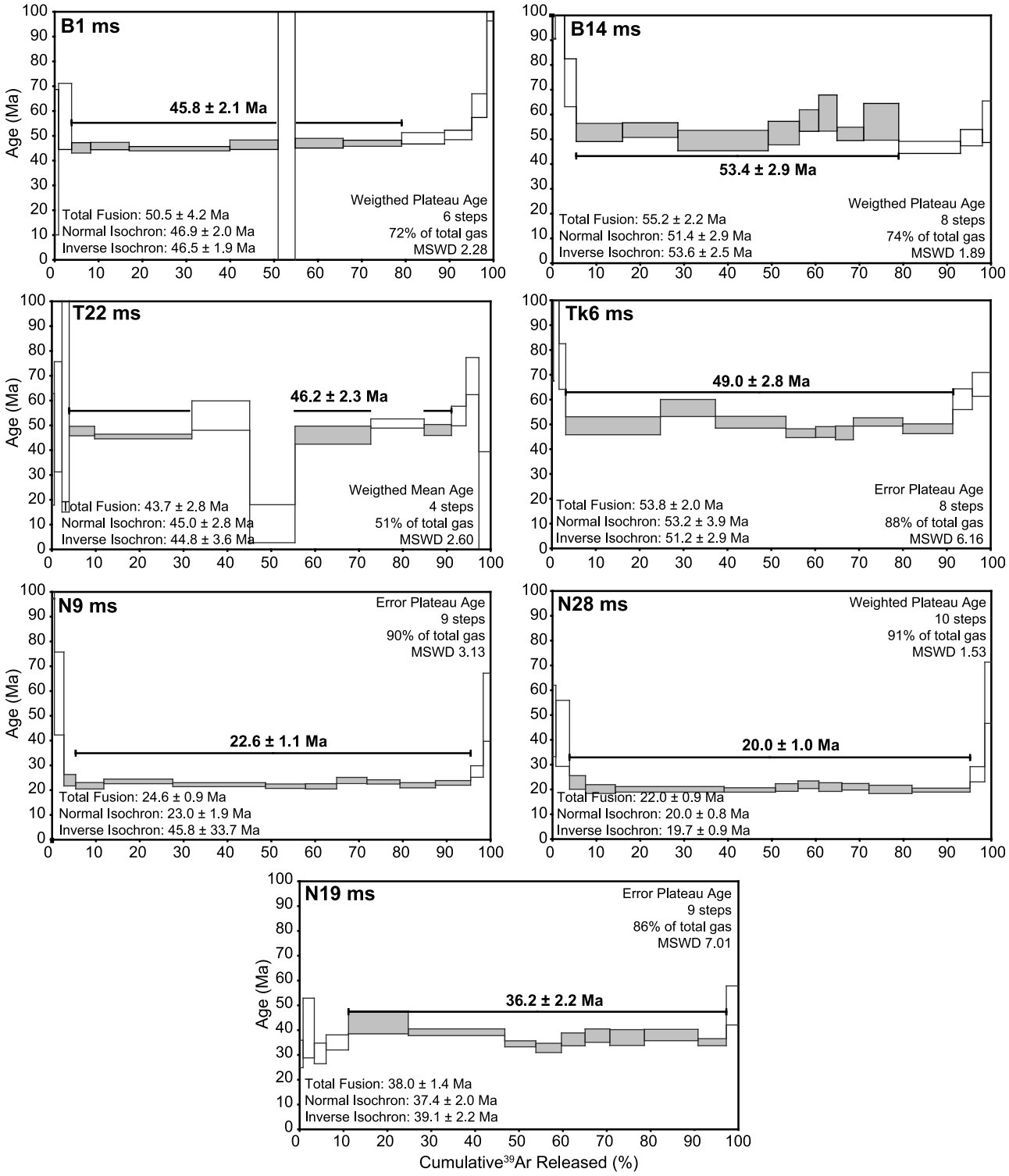

Figure 8. The $^{40}Ar/^{39}Ar$ age spectra from furnace step heating experiments on seven muscovite samples. The bold ages are error-weighted plateau ages or error plateau ages including internal and external errors as described in section A1. The gray steps are the ones which were included in the age calculation.

in the matrix and is interpreted to have formed during crystallization of the igneous rocks. One muscovite sample was collected from the schist zone in the Tokio transect and is exposed close to a major intrusion (Tk6; Figure 2c). This sample is affected by contact metamorphism and the development of its muscovite flakes is contemporary to the intrusion: coarse muscovite and fine-grained sillimanite statically replace andalusite crystals. The other three muscovite samples (T22, N9, N28) were collected from the gneiss zone in the Tana and Nunatak transects (Figure 2). In

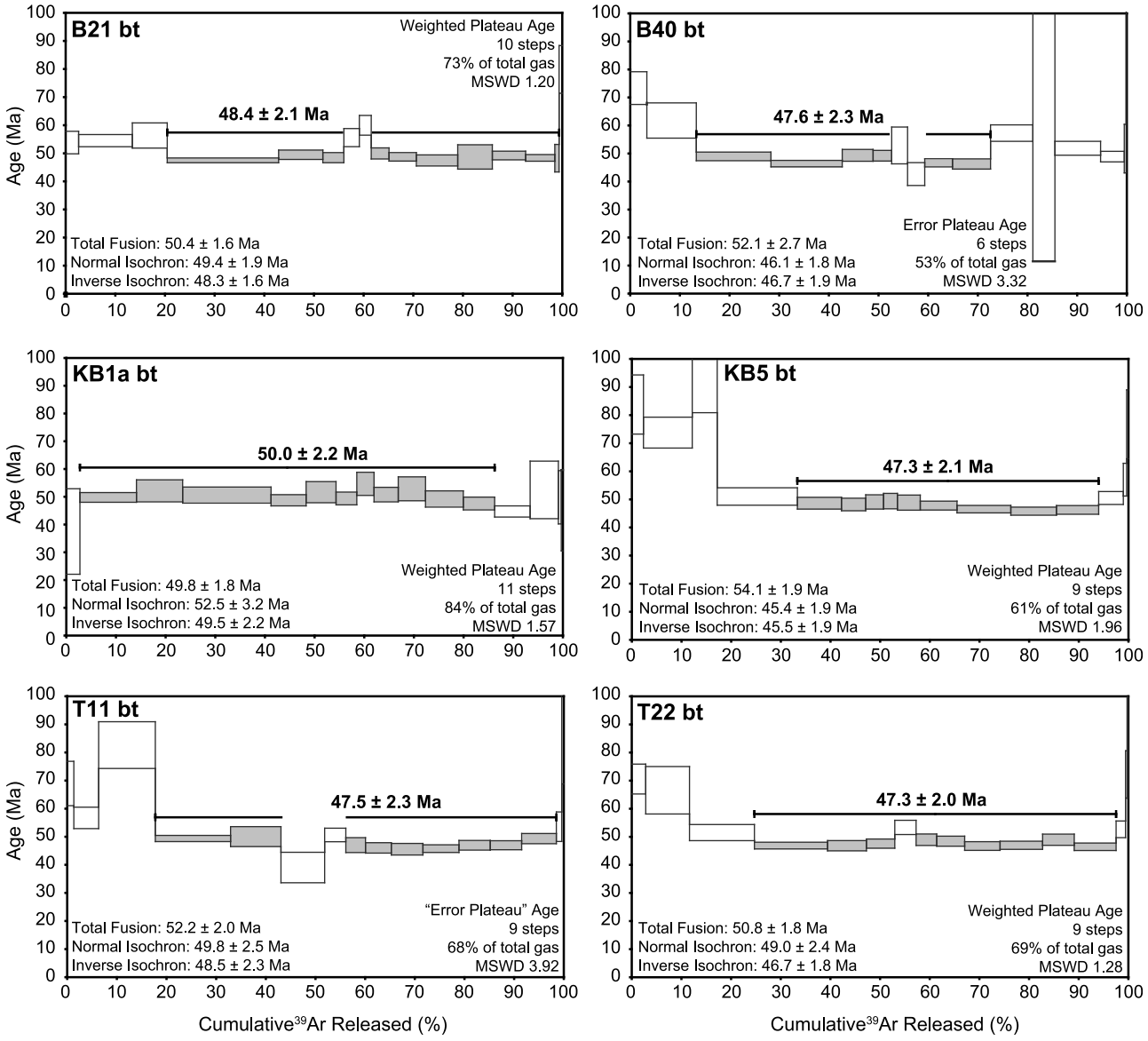

Figure 9. The $^{40}Ar/^{39}Ar$ age spectra from furnace step heating experiments on 12 biotite samples. The bold ages are error-weighted plateau ages or error plateau ages including internal and external errors as described in section A1. The gray steps are the ones which were included in the age calculation.

all three samples, muscovite is aligned parallel to S_{melt} and probably grew before or at the metamorphic peak.

[24] One of the 12 biotite-bearing samples was collected from the schist zone of the Bremner transect (B40; Figure 2b). In this sample, fine-grained biotite, containing many opaque inclusions, defines S_{bt}. Another biotite-bearing sample was collected from the large intrusion exposed at the southern end of the Tokio transect (Tk7; Figure 2c). In this sample, coarse biotite is randomly oriented in the matrix. The remaining 10 biotite-bearing samples are all from gneisses distributed through the gneiss zone of the CMC (Figures 2 and 7). In all of these gneiss samples, biotite mainly defines S_{bt}. In some cases, newly grown biotite also occurs parallel to S_{melt}. All biotites have a relatively constant composition of ~50%–60% annite and ~40%–50% phlogopite [*Bruand*, 2011].

[25] The sample preparation process and the analytical technique is described in section A1, detailed isotopic measurements can be found in Data Sets S1 and S2, and the results of the step heating experiments are displayed as age spectra in Figures 8 and 9. Weighted plateau or error plateau ages (section A1 [*Koppers*, 2002]), the total fusion, normal and inverse isochron ages are given in each diagram. Errors are quoted at 2 sigma.

[26] For the muscovite samples, weighted plateau ages consisting of subsequent degassing steps comprising >50% of the total gas could be calculated for samples B14 and N28 (Figure 8). For sample B1 a weighted plateau age could be calculated after excluding one step which had a very high analytical error. Sample T22 gave a more discordant age spectra for which we calculated a weighted mean age after excluding three intermediate steps. The other three samples

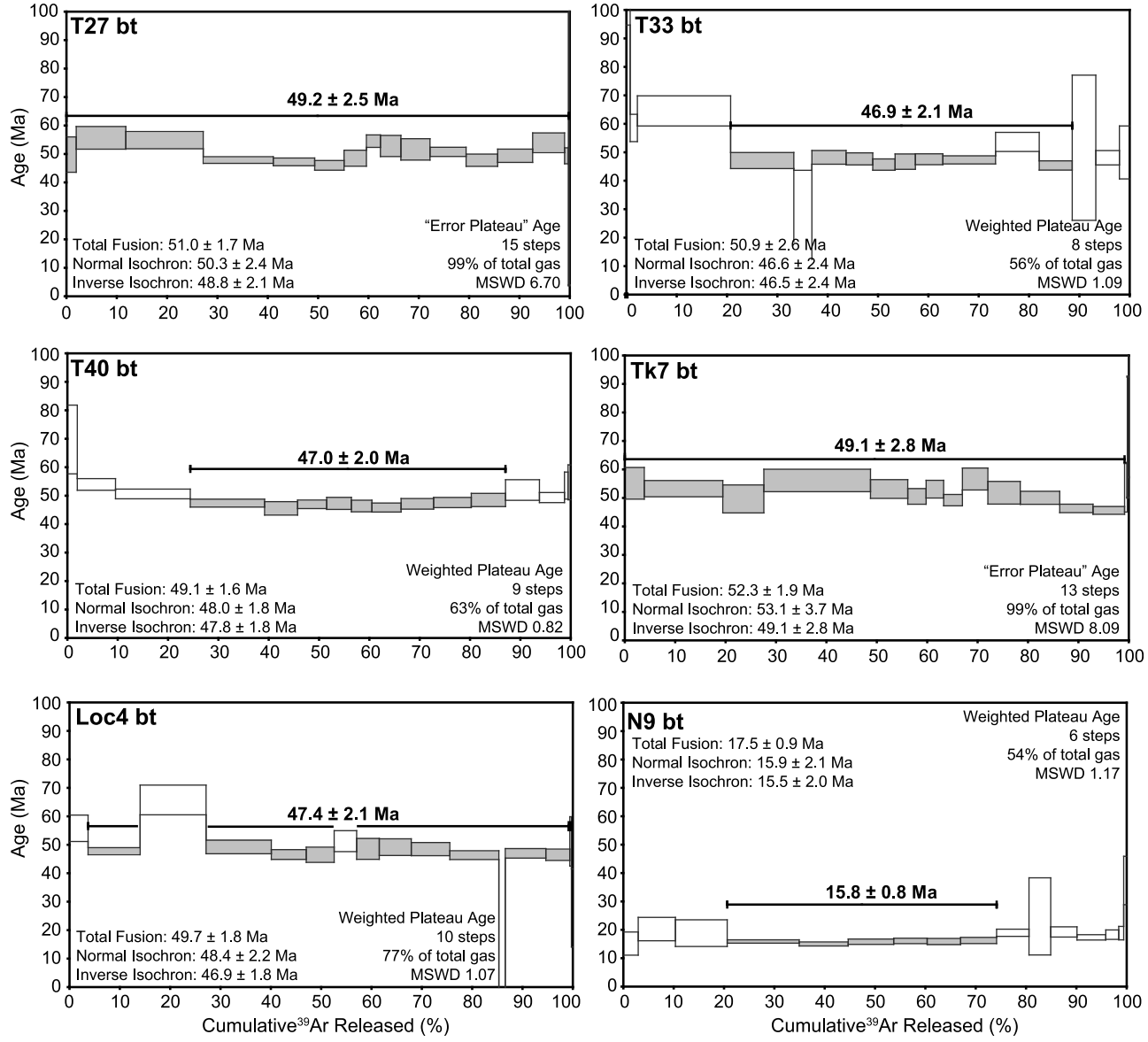

Figure 9. (continued)

Tk6, N9 and N19 did not yield statistically significant weighted plateau ages, and error plateau ages are reported (calculated using the work by *Koppers* [2002]). Muscovite ages from sections 1 and 2 of the CMC range from 53.4 ± 2.9 Ma to 45.8 ± 2.1 Ma (±2 sigma), but only one sample (B41) is older than circa 50 Ma, with the remaining samples giving ages less than circa 49 Ma (Table 1 and Figure 8). Muscovite samples from section 3, however, give significantly younger ages ranging from 36.2 ± 2.2 Ma to 20.0 ± 1.0 Ma (Table 1 and Figure 8).

[27] For the biotite samples, weighted plateau ages consisting of subsequent degassing steps comprising >50% of the total gas could be calculated for samples KB1a, KB5, T40 and N9 (Figure 9). Weighted plateau ages could be calculated for samples B21, T22, T33 and Loc 4 after excluding one to two intermediate steps (Figure 9). No statistically meaningful weighted plateau ages could be calculated for samples B40, T11, T27, and Tk7 and error plateau ages are reported for these samples (Figure 9). Biotite ages from sections 1 and 2 of the CMC range from 50.0 ± 2.2 Ma to 46.9 ± 2.1 Ma, which is within error of the ages from the muscovites for those regions (Table 1 and Figure 9). The only biotite age from section 3 is much younger with 15.8 ± 0.8 Ma, which is younger than the youngest muscovite age from this region.

4.2.2. Rb/Sr Isochron Dating

[28] To further evaluate the validity of the $^{40}Ar/^{39}Ar$ weighted plateau and error plateau ages as cooling ages, we also dated 7 of the 12 biotite separates used for $^{40}Ar/^{39}Ar$ dating and one additional biotite-bearing sample from section 3 by the Rb/Sr method, based on two point isochrons derived from biotite and whole rock measurements, respectively. The analytical technique is described in section A2, detailed isotopic measurements can be found in Data Set S3,

the ages are reported in Table 1 and the isochron plots are displayed in Figure 10. Errors are quoted at ±95% confidence interval. The six Rb/Sr ages from sections 1 and 2 vary between 50.3 ± 0.5 Ma and 48.5 ± 0.5 Ma, whereas the two Rb/Sr ages from section 3 are both 14.9 ± 0.2 Ma (Table 1). All Rb/Sr ages lie within error of the $^{40}Ar/^{39}Ar$ ages of the biotites, independently of whether the plateau age was a weighted or an error plateau age (Table 1). Assuming similar closure temperature ranges for the two systems, this indicates that the $^{40}Ar/^{39}Ar$ ages are meaningful and do not represent a mixing of gas reservoirs, inheritance, loss or excess of argon.

4.2.3. Zircon Fission Track Dating

[29] We analyzed four samples from sections 1 and 2 by the zircon fission track method in order to extrapolate the cooling history between the U/Pb, $^{40}Ar/^{39}Ar$ and Rb/Sr cooling ages and the published low-temperature thermochronology. The analytical technique is described in section A3. Ages are reported in Table 1, and detailed information is given in Data Set S4. Samples B21, T40 and Loc4 yielded 17–20 datable zircon grains. All three samples pass the χ^2 test, indicating that the grains belong to one single age population, and central ages for all three samples lie within error of each other (26.0 ± 2.8 Ma to 28.9 ± 2.4 Ma; Table 1). Sample 91ASn11 yielded only two datable grains (36 ± 6 Ma and 24 ± 5 Ma) which fall well within the single grain age range of the three aforementioned samples.

4.3. Construction of Cooling Paths

4.3.1. Closure Temperature Estimates

[30] The geochronological data presented above (Table 1 and Figure 7) allow the construction of cooling paths for the different parts of the metamorphic complex (Figure 11). Low-temperature geochronological data is generally interpreted as representing cooling through the following temperature ranges (Figure 11): 200°C–300°C for zircon fission track ages [e.g., *Wagner and van den Haute*, 1992], 160°C–200°C for zircon (U-Th)/He ages [e.g., *Reiners et al.*, 2003], 60°C–120°C for apatite fission track ages [e.g., *Green et al.*, 1986; *Carlson et al.*, 1999], and 40°C–80°C for apatite (U-Th)/He ages [e.g., *Wolf et al.*, 1996].

[31] The interpretation of $^{40}Ar/^{39}Ar$ and Rb/Sr ages in deformed metamorphic rocks in terms of cooling is less straightforward [e.g., *Jenkin*, 1997; *Villa*, 1998], since the ages could either represent cooling below a certain temperature [e.g., *Dodson*, 1973], and/or recrystallization of the mineral due to deformation or fluid-rock interaction [e.g., *Dunlap*, 1997; *Villa*, 1998]. In our samples, the ages probably represent cooling ages for two major reasons: (1) the muscovite and biotite ages obtained from undeformed intrusive rocks are indistinguishable from ages in the surrounding country rocks, and these igneous samples show no evidence of retrograde recrystallization or fluid-rock interactions, and (2) most of the samples were obtained from metamorphic rocks with high-grade fabrics which equilibrated at temperatures of >600°C, far above the closure temperatures for muscovite or biotite, and which show no signs of later recrystallization or alteration due to fluid flow.

[32] Closure temperatures for $^{40}Ar/^{39}Ar$ and Rb/Sr ages vary considerably depending on cooling rate, grain size, pressure, and diffusion coefficients [e.g., *Dodson*, 1973; *Dahl*, 1996; *Jenkin*, 1997; *McDougall and Harrison*, 1999; *Harrison et al.*, 2009]. In our samples, grain sizes for muscovite and biotites in the separates are ~100–500 μm, the maximum metamorphic pressures are ~5–10 kbar, and the mineral chemistry is homogenous [*Bruand*, 2011]. $^{40}Ar/^{39}Ar$ cooling ages from sections 1 and 2 lie very close to the U/Pb ages for peak metamorphism, suggesting first-order cooling rates to mica closure on the order of ~50°C–100°C/Ma. In contrast, $^{40}Ar/^{39}Ar$ ages from section 3 are considerably younger than the peak metamorphic ages estimated from U/Pb methods, suggesting that the high-temperature cooling rate was on the order of ~5°C–10°C/Ma. Thus, based on *Harrison et al.*'s [2009] experiments, we assume a closure temperature range for the muscovite samples of sections 1 and 2 of 430°C (100 μm grain at 50°C/Ma and 5 kbar) to 495°C (500 μm grain at 100°C/Ma and 5 kbar), and for the samples of section 3 of 395°C (100 μm grain at 5°C/Ma and 5 kbar) to 455°C (500 μm grain at 10°C/Ma and 5 kbar).

[33] For the closure temperature of $^{40}Ar/^{39}Ar$ in biotite, we use the equation of *Dodson* [1973] and the diffusion parameters given by *McDougall and Harrison* [1999] for biotites of similar composition (~Ann_{60}, E = 47 kcal/mol, D_0 = 0.075 cm^2/s, cylindrical geometry) to estimate the closure temperature for our samples. For the samples of sections 1 and 2, we calculate a closure temperature range of 340°C (100 μm grain at 50°C/Ma) to 412°C (500 μm grain at 100°C/Ma). For the samples of section 3 we calculate a closure temperature range of 307°C (100 μm grain at 5°C/Ma) to 370°C (500 μm grain at 10°C/Ma). Since the Rb/Sr isochron ages lie within error of the $^{40}Ar/^{39}Ar$ biotite ages we assume a similar closure temperature range for this system.

[34] For the closure temperatures of the two $^{40}Ar/^{39}Ar$ hornblende ages from the literature [*Sisson et al.*, 1989, 2003], we assume ranges of 500°C–550°C for sections 1 and 2 (cooling rates of 50°C–100°C/Ma, grain size 40–80 μm) and 460°C–510°C for section 3 (cooling rates of 5°C–10°C/Ma, grain size 40–80 μm [*McDougall and Harrison*, 1999]). For the only $^{40}Ar/^{39}Ar$ plagioclase age, we assume a range of 150°C–210°C [*Sisson et al.*, 1989].

4.3.2. Cooling Histories

[35] Figures 11a and 11b show the cooling curves for sections 1 and 2 of the CMC. U/Pb zircon ages (Table 1 [*Gasser*, 2010]) together with peak temperatures derived by classical thermometry for the dated samples (Figure 2) define the starting point for the cooling history. $^{40}Ar/^{39}Ar$ hornblende, muscovite and biotite ages define a steep cooling curve right after the metamorphic peak in both sections (red part of cooling curve; Figures 11a and 11b). During this phase, the rocks cooled from ~650°C–700°C at ~55–52 Ma to ~350°C–400°C at ~50–46 Ma, resulting in cooling rates between 29°C/Ma and 180°C/Ma. The second phase of the cooling history shows an evolution from north to south within the area of sections 1 and 2. Rocks of the phyllite and schist zones in the north of the complex probably cooled relatively rapidly to near-surface temperatures already in the Eocene (oldest apatite fission track ages from the schist zone are ~40 Ma). Rocks of the gneiss zone farther south, however, experienced a prolonged period (~15–20 Ma, yellow part of cooling history; Figures 11a and 11b) at temperatures of ~300°C–400°C and only started cooling through the zircon fission track closure temperature around ~30–25 Ma. Parts of the southernmost

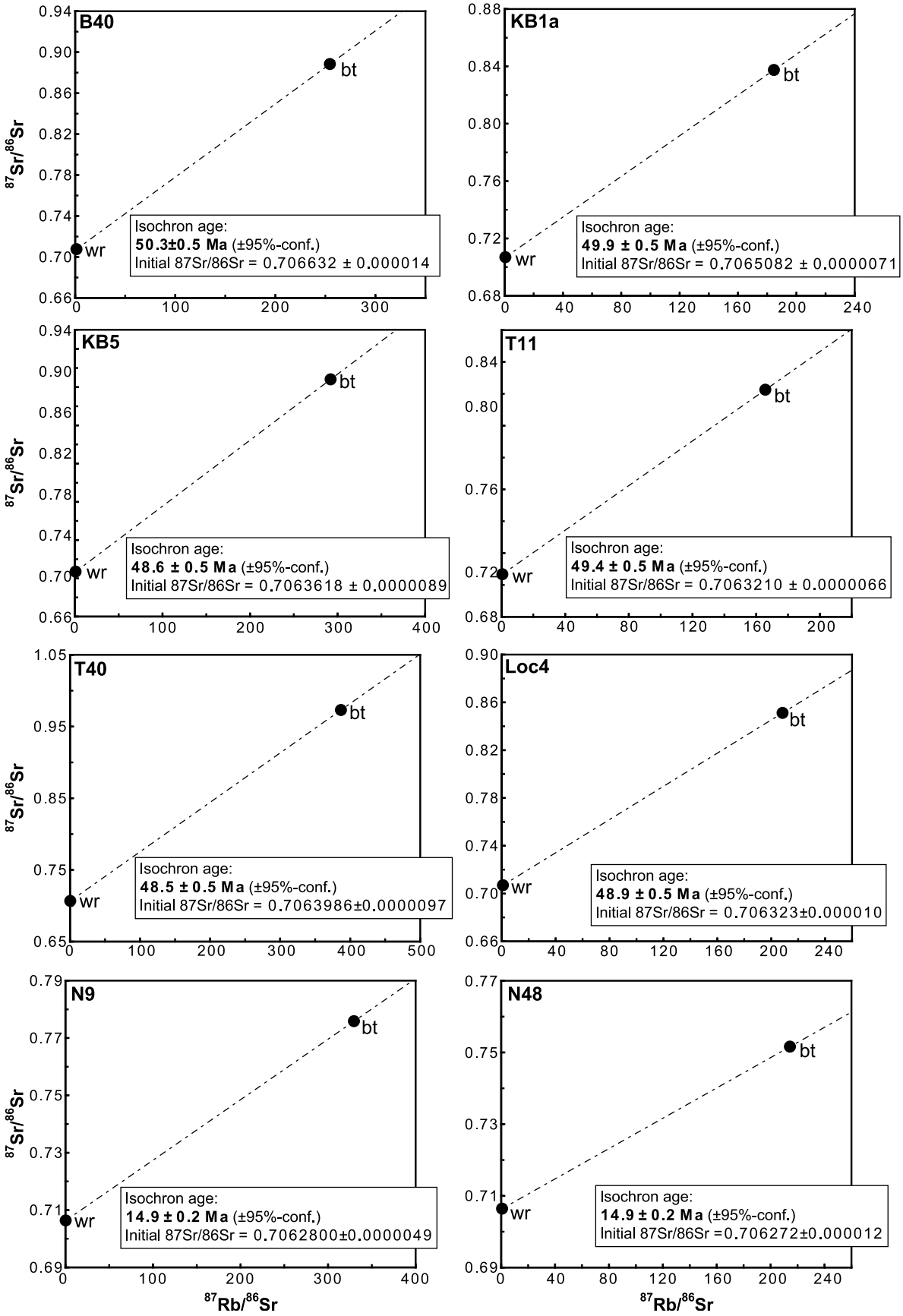

Figure 10. Rb-Sr isochrons for biotite (bt) and whole rock (wr) measurements. Analytical techniques are described in section A2.

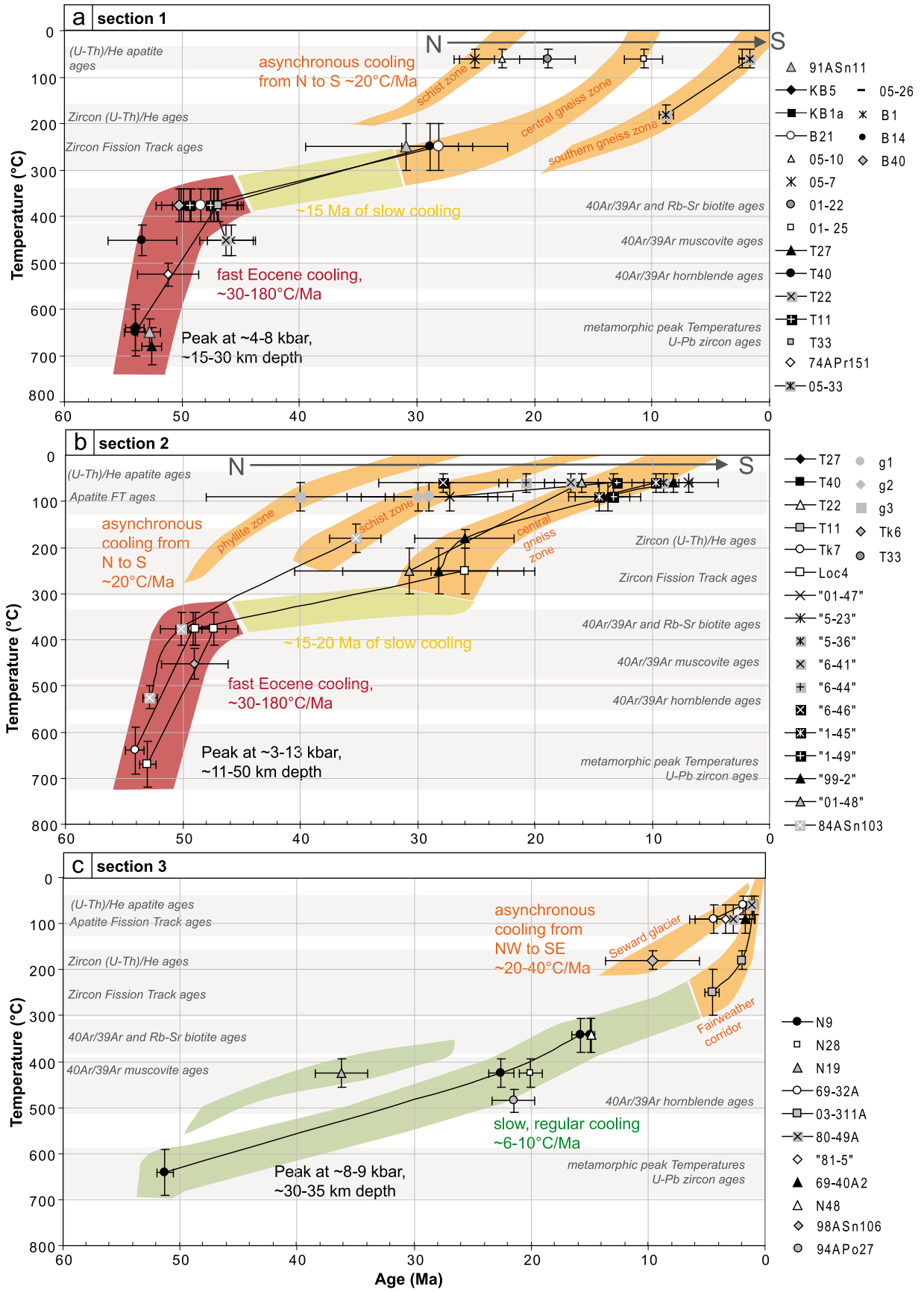
a section 1
(U-Th)/He apatite ages
Zircon (U-Th)/He ages
Zircon Fission Track ages
asynchronous cooling from N to S ~20°C/Ma
N
S
schist zone
central gneiss zone
southern gneiss zone
~15 Ma of slow cooling
fast Eocene cooling, ~30-180°C/Ma
Peak at ~4-8 kbar, ~15-30 km depth
40Ar/39Ar and Rb-Sr biotite ages
40Ar/39Ar muscovite ages
40Ar/39Ar hornblende ages
metamorphic peak Temperatures U-Pb zircon ages
91ASn11
KB5
KB1a
B21
05-10
05-7
01-22
01- 25
T27
T40
T22
T11
T33
74APr151
05-33
05-26
B1
B14
B40
b section 2
(U-Th)/He apatite ages
Apatite FT ages
asynchronous cooling from N to S ~20°C/Ma
phyllite zone
schist zone
central gneiss zone
~15-20 Ma of slow cooling
fast Eocene cooling, ~30-180°C/Ma
Peak at ~3-13 kbar, ~11-50 km depth
Zircon (U-Th)/He ages
Zircon Fission Track ages
40Ar/39Ar and Rb-Sr biotite ages
40Ar/39Ar muscovite ages
40Ar/39Ar hornblende ages
metamorphic peak Temperatures U-Pb zircon ages
T27
T40
T22
T11
Tk7
Loc4
"01-47"
"5-23"
"5-36"
"6-41"
"6-44"
"6-46"
"1-45"
"1-49"
"99-2"
"01-48"
84ASn103
g1
g2
g3
Tk6
T33
c section 3
(U-Th)/He apatite ages
Apatite Fission Track ages
Zircon (U-Th)/He ages
Zircon Fission Track ages
40Ar/39Ar and Rb-Sr biotite ages
40Ar/39Ar muscovite ages
asynchronous cooling from NW to SE ~20-40°C/Ma
Seward glacier
Fairweather corridor
slow, regular cooling ~6-10°C/Ma
Peak at ~8-9 kbar, ~30-35 km depth
40Ar/39Ar hornblende ages
metamorphic peak Temperatures U-Pb zircon ages
N9
N28
N19
69-32A
03-311A
80-49A
"81-5"
69-40A2
N48
98ASn106
94APo27
Temperature (°C)
Age (Ma)

Figure 11

gneiss zone even stayed at elevated temperatures of >200°C until ~10 Ma [e.g., *Enkelmann et al.*, 2008, 2010]. The slope of the orange cooling curves lies in the range of ~20°C/Ma.

[36] The cooling history for section 3 is significantly different from those of sections 1 and 2 (Figure 11c). The starting point is defined by a U/Pb zircon age of ~51 Ma (Table 1) corresponding to a maximum temperature of ~600°C–700°C (Figure 2). $^{40}Ar/^{39}Ar$ hornblende, muscovite, biotite and zircon fission track ages define a slow, regular cooling curve from the peak conditions down to 200°C–300°C until circa 5 Ma (green part of cooling curve; Figure 11c). This corresponds to a cooling rate of ~6°C–10°C/Ma. The young zircon fission track and zircon and apatite (U-Th)/He ages from the Fairweather corridor indicate a strong increase in cooling rate during the last ~5 Ma, with rates of 20°C–40°C/Ma, consistent with their locations within the obliquely convergent part of the St. Elias orogen (orange part of cooling curve [*Pavlis et al.*, 2004; *Enkelmann et al.*, 2010]). The slightly older zircon (U-Th)/He age from Seward glacier indicates a somewhat slower cooling, but the <3 Ma zircon fission track ages found in river sands draining the Seward glacier area [*Enkelmann et al.*, 2009, 2010] indicate that the entire strip from Seward glacier down to Nunatak fjord (Figure 2a) experienced rapid cooling during the last ~5 Ma.

5. Tectonic Evolution of CMC

[37] The structural history, metamorphic evolution and thermochronological data summarized above allow a discussion of the tectonic evolution of the CMC in space and time. Our study generally supports the structural succession D_1–D_3 for the CMC (Figure 5) that has been recognized previously by *Pavlis and Sisson* [1995, 2003]. D_1 formed during the initial accretion of the sediments, whereas D_2 and D_3 are related to metamorphism in the CMC. In the following, the structural record, the metamorphic evolution and the cooling and exhumation histories of the CMC are integrated and a possible tectonic evolution for the entire complex is presented in a regional context.

5.1. D_1: Accretion of Sediments

[38] The D_1 deformation is related to the accretion of sediments to the continental margin during Late Cretaceous–Paleocene times [e.g., *Plafker et al.*, 1994]. At that time, a large accretionary prism formed which derived its sediments probably mostly from the Coast Plutonic Complex, a large continental margin magmatic arc which is exposed to the southeast of the present location of the accretionary prism (Figure 1a [e.g., *Nilsen and Zuffa*, 1982; *Farmer et al.*, 1993; *Sample and Reid*, 2003; *Haeussler et al.*, 2005]). At the same time, the Border Range Fault System was reactivated as a large-scale dextral strike-slip system [*Pavlis and Roeske*, 2007]. The accretionary prism therefore represented a transpressive system with the convergent component distributed on thrusts and folds within the prism and the strike-slip component concentrated on the border of the prism. The accretionary prism probably either formed on the Farallon plate, and later moved dextrally across the Kula-Farallon ridge (Figure 1d [e.g., *Cowan*, 2003]), or it formed on the Resurrection plate, which finally completely subducted below the margin (Figure 1d [e.g., *Haeussler et al.*, 2003]). In both cases, the convergence between the oceanic plate and the continent must have been dextrally oblique in order to produce the strain-partitioned transpressional D_1 deformation.

[39] Such accretionary and subduction zone settings are generally relatively cold, with typical geothermal gradients of ~10°C–15°C/km, leading to blueschist facies metamorphism at depths of ~15–20 km [e.g., *Philpotts and Ague*, 2009]. However, given the widespread distribution of subgreenschist facies to greenschist facies conditions all along the Chugach accretionary prism [e.g., *Dusel-Bacon*, 1994], the initial geothermal gradient in this prism was probably on the order of ~20°C–25°C/km, resulting in conditions of ~300°C–500°C at depths of ~15–20 km (~4–6 kbar). One possible explanation for this elevated initial geothermal gradient in the accretionary prism is that it is the result of the subduction of a spreading ridge below the margin, related to the intrusions of the Sanak-Baranof plutonic belt [e.g., *Sisson et al.*, 1989; *Sisson and Pavlis*, 1993]. However, the thermal structure of an accretionary prism depends on many factors such as the amount of accretion and erosion, the coefficient of basal friction, shear heating at the base, internal strain heating and the pore fluid/lithostatic pressure ratio [e.g., *Barr and Dahlen*, 1989]. Examples of relatively high thermal gradients of ~20°C–25°C/km in accretionary prisms without the involvement of a subducting ridge include the Taiwan accretionary prism [*Barr and Dahlen*, 1989] or the Cascadia accretionary wedge [*Booth-Rea et al.*, 2008].

5.2. D_2: Vertical Flattening and Margin-Parallel Stretching

[40] After accretion and D_1 deformation during oblique convergence, the deeper parts of the accretionary prism in the area of the future CMC were subjected to D_2 deformation: the presence of the flat-lying D_2 fabric accompanied by a pronounced orogen-parallel stretching lineation indicates that the base of the accretionary prism experienced vertical thinning and margin-parallel stretching [e.g., *Pavlis and Sisson*, 1995]. The D_2 fabric formation was accompanied by andalusite-grade metamorphism just above the D_2 fabric front, sillimanite-grade metamorphism within the schist and parts of the gneiss zone and culminated in the onset of partial melting in the gneiss zone. The vertical thinning during D_2 probably led to the compression of isotherms and

Figure 11. (a–c) Cooling curves for the three different sections of the CMC (Figure 7) as derived from the combination of different thermochronological methods. Black lines connect data points derived by different methods for the same sample. The sample localities are shown in Figure 7. Red indicates the rapid Eocene cooling phase which occurred in sections 1 and 2 directly after the metamorphic peak. Yellow indicates the prolonged period (15–20 Ma) of slow/no cooling in the gneiss zone of sections 1 and 2 of the CMC. Green indicates the slow, regular cooling from peak conditions down to 200°C–300°C in section 3. Orange indicates cooling curves for the final cooling from 200°C–300°C to near-surface temperatures in all sections. In sections 1 and 2, this orange cooling occurred asynchronous from north to south across the complex.

to the presence of relatively high geothermal gradients in the lowermost phyllite, the schist and gneiss zones. *Sisson and Hollister* [1988] and *Sisson et al.* [1989] derived thermal gradients of ~35°C/km for the northern schist zone and ~65°C/km for the westernmost gneiss zone of the complex. *Sisson and Pavlis* [1993] and *Pavlis and Sisson* [1995] suggested that this could be the result of a second passage of a triple junction, which first caused the initial high geothermal gradient during southward migration, and than caused the even higher gradients during northward migration. However, an increase from ~25°C/km during D_1 to ~35°C–65°C/km during D_2 at depths of ~10–20 km could also be the result of a total vertical thinning of ~6–10 km of the crustal column. Finite strain modeling of *Pavlis and Sisson* [1995] showed that depending on the ratio of pure to simple shear during D_2 deformation ~2–7 km of vertical thinning could have occurred alone in the D_2 fabric of the schist zone, making a total of ~6–10 km thinning in the entire D_2 zone a realistic value. Based on these considerations, the D_2 vertical shortening probably could have been sufficient to produce the high geothermal gradients observed in the northern and western parts of the complex. In addition, the central and eastern parts of the gneiss zone show lower geothermal gradients of 15°C–30°C/km due to higher metamorphic pressures [*Bruand*, 2011], making a second passage of a triple junction below the complex unlikely.

[41] The peak metamorphic conditions are constrained to ~55–51 Ma (Table 1 [*Gasser*, 2010]). The D_2 deformation therefore must have started at about the same time or shortly before. This period is broadly contemporaneous with a plate tectonic reorganization in the Pacific basin (chron 24–21, ~53–48 Ma [*Atwater*, 1989]) suggesting that there might be a relationship between movements of the oceanic plates in the Pacific basin and the strain history along the margin [*Sisson and Pavlis*, 1993; *Pavlis and Sisson*, 1995]. However, since it is not well constrained what exactly happened during this reorganization [e.g., *Byrne*, 1979; *Engebretson et al.*, 1985; *Lonsdale*, 1988; *Atwater*, 1989; *Norton*, 1995], great freedom remains in interpreting the resulting boundary forces which acted on the margin. D_2 could, for example, be the result of a short-lived transtensional event due to a short-term change in movement direction of the plate segment which was subducting below the margin, related to the plate reorganization. Or it could be the result of forces which acted inside the accretionary prism: after a decrease in convergence rate due to the plate reorganization, gravitational collapse of the overthickened accretionary prism could have occurred leading to the D_2 stretching and vertical thinning. However, in this case extension perpendicular to the margin rather than parallel to it would be expected.

[42] Other possible reasons for D_2 deformation are not directly linked with the plate reorganization. *Sisson and Pavlis* [1993] and *Pavlis and Sisson* [1995] for example suggested that the subduction of an oceanic spreading ridge below the margin could have caused the D_2 deformation, with the subduction of the ridge topography inducing the vertical thinning component. The subduction of a ridge below the margin at the time of interest has been inferred by many workers and depending on where to restore the accretionary prism along the margin, potential candidates are the ridge between the Kula and Farallon plates (Figure 1d) [e.g., *Bradley et al.*, 1993; *Sisson and Pavlis*, 1993; *Pavlis and Sisson*, 1995; *Haeussler et al.*, 1995]) or the ridge between the Kula and Resurrection plates (Figure 1d [e.g., *Haeussler et al.*, 2003]). Alternatively, *Pavlis and Sisson* [2003] explored the possibility of D_2 and D_3 actually being the result of the same dextral transpressive deformation, with D_2 representing a midcrustal decoupling horizon. Or, D_2 could be the result of underplating of a buoyant package of off-scraped sedimentary rocks and oceanic crust below the accretionary prism (as it is indicated by seismic profiles crossing Prince William Sound; Figure 1 [e.g., *Fuis et al.*, 2008]). As a last possibility, the D_2 deformation could have been caused by the geometry of the margin itself: it could be the result of the accretionary prism sliding past a releasing bend in the large-scale strike-slip system bordering the prism.

5.3. D_3: Dextral Transpression

[43] From D_2 to D_3, a switch from vertical thinning to horizontal shortening and the onset of dextral shearing occurred. A dextral transpressive shear system developed which heterogeneously affected the entire area. In the schist zone, open folding, crenulation foliation development and semibrittle to brittle dextral fault zones developed, probably associated with fast cooling due to a relaxation of the isotherms after the thinning of D_2 ceased. In the gneiss zone, high-temperature deformation continued and domains of high and low D_3 dextral transpressive shear developed. The D_3 deformation is concentrated along the southern border of the CMC in sections 1 and 2: in the southern gneiss zone (southern end of the Fan transect, the entire Tana transect and large parts of the Bagley transect; Figure 3) D_3 is dominant and the D_2 fabric is mostly transposed into the steep D_3 fabric. In addition to the higher intensity, the stretching lineation on the D_3 fabric also plunges 30°–60° to the west-northwest in these southern parts, in contrast to the lineation in the northern parts where it is subhorizontal. Simultaneously with the D_3 deformation, partial melting occurred extensively in the gneiss zone and melts rose along the D_3 foliation planes to form bigger plutons which intruded the schist zone, and which locally thermally overprinted the andalusite-grade metamorphism present above the D_2 fabric front in the schist zone in section 2.

[44] The domains with high D_3 fabric intensity and down-dip lineations correspond to the domains which registered higher peak pressures than the rest of the complex (~7–8 kbar at the Tana transect, ~8–13 kbar at the Bagley transect; Figures 2b and 2c), which suggests that the higher pressures are related to this D_3 deformation. We therefore interpret that during this dextral transpressive deformation, rocks of the gneiss zones were partly exhumed along north dipping D_3 foliation planes with down-dip lineations. This process may represent a narrow extrusion channel in which exhumation occurred due to focused erosion at the surface. Such erosion might have been a consequence of the shortening component of the D_3 deformation, which was concentrated in the southern gneiss zone and along the Contact fault and leading to the formation of topography at the surface. There is, in fact, significant evidence for erosion during the Early Eocene in the Chugach terrane. Approximately 100 km west of the CMC, Early Eocene nonmarine sedimentary basins unconformably overlie the Chugach terrane [e.g., *Little and Naeser*, 1989]. These sedimentary rocks record a proximal

metasedimentary and metavolcanic source from the Chugach Mountains, forming large alluvial fan complexes [*Little and Naeser*, 1989; *Trop and Ridgway*, 2007].

[45] The D_3 deformation with its dextral transpression is typical for what has been the situation along the margin already during the formation of the accretionary prism during D_1. It therefore represents a switch back after the unusual D_2 event to a normal deformational regime with oblique subduction of oceanic plates below the continental margin. During accretion of the sediments, the strike-slip component of deformation was localized mainly along the Border Range Fault System inboard of the accretionary prism (termed the Hanagita Fault System; Figure 1b [*Roeske et al.*, 2003; *Pavlis and Roeske*, 2007]). During the renewed dextral transpression of D_3, this deformation concentrated farther outboard, along the Contact Fault system and within the gneissic core of the CMC. This outboard jump and concentration of dextral transpression could be related to the fact that the accretionary prism was enlarged due to the accretion of the Prince William terrane which is located outboard of the Chugach terrane.

[46] The cooling histories of the different sections of the complex are related to this D_3 deformation. The western and central sections show very fast cooling shortly after the metamorphic peak (Figure 11). This cooling could (1) be related to passive thermal relaxation after the passage of a subducting ridge [e.g., *Sisson and Pavlis*, 1993; *Pavlis and Sisson*, 1995; *Bradley et al.*, 2003] and/or (2) be the result of fast exhumation of hot material into colder regions during D_3 transpression. In the case of passive cooling, a very fast removal of the heat source at depth is required. This is unlikely in a plate geometry as shown by *Haeussler et al.* [2003] and *Madsen et al.* [2006] where the Kula-Resurrection ridge is subducting parallel to the margin below the CMC. Moreover, thermal modeling of *Groome and Thorkelson* [2009] showed that for a slowly migrating triple junction (10 mm/yr), the effect of ridge subduction is characterized by a protracted metamorphic heating followed by slow cooling, particularly at depths of >20 km, which is not observed in sections 1 and 2 of the CMC. Therefore, if a ridge was subducting below the CMC during Eocene times, it must have moved fast, and the plate tectonic geometry must have been in such a way that old and cold lithosphere was subducted shortly after the passage of the ridge in order to cool the rocks quickly. Since subduction velocities at that time were relatively high (100 mm/yr or more [*Doubrovine and Tarduno*, 2008]), and a major plate tectonic reorganization occurred simultaneously to metamorphism in the CMC, such a scenario with a fast moving triple junction could have taken place [*Sisson and Pavlis*, 1993; *Pavlis and Sisson*, 1995, 2003]. However, due to uncertainties in the plate tectonic configuration this scenario is poorly constrained.

[47] It is likely that the fast cooling after the metamorphic peak in the western and central parts of the complex was the result of additional exhumation of at least parts of the gneiss zone for the following reason. Peak pressures reported by these rocks correspond to depths of ~20–50 km, and if only passive cooling would have occurred after the peak, then all of the exhumation from this depth to the surface must have occurred during later stages of the cooling history (from ~350°C to the surface), notably after ~25 Ma (Figure 11). This would imply an unrecognized massive exhumation of parts of the gneiss zone in the Neogene. In addition it would require that the exhumation took place entirely during relatively low temperatures and therefore along semibrittle to brittle faults. However, the ductile penetrative steep foliation with down-dip lineations developed in the gneisses where the highest pressures are recorded indicate that at least parts of the exhumation took place during ductile deformation shortly after the metamorphic peak. Therefore, at least for the zones where relatively high pressures are reported, the metamorphic peak was followed by exhumation. After the fast cooling phase recorded in sections 1 and 2 of the CMC, both the gneiss and schist zones were probably at similar depths of ~10–15 km, and the remaining exhumation occurred asynchronously from north to south, with the schist zone reaching relatively shallow depths already in the Eocene, whereas the southern gneiss zone stayed at considerable depths until ~10 Ma ago (e.g., in a mechanism similar to that described by *Enkelmann et al.* [2008, 2010]).

[48] Despite similar structural observations and similar metamorphic grade, the cooling and exhumation history of the southeastern section of the complex is different from the western and central sections. Cooling and exhumation occurred much slower and more regularly in the southeastern section from the metamorphic peak until relatively recent times (Figure 11). We suggest that this difference is the result of the postmetamorphic tectonic configuration of these two segments along the margin, an interpretation which has important implications for the paleogeometry of the margin. Specifically, it has long been suggested from paleomagnetic data [*Coe et al.*, 1985, 1989] and the geology of the southern Alaska margin [*Nokleberg et al.*, 1989] that the Alaskan orocline (i.e., the curvature of the present-day margin) was in existence by Eocene time. Our results provide independent support for this interpretation. If the margin was already curved during cooling and exhumation of the three sections, and the Pacific plate moved northwestward relative to North America as indicated by plate tectonic reconstructions [e.g., *Doubrovine and Tarduno*, 2008], then the western and central parts of the complex were under constant convergence after peak metamorphism. This ongoing convergence may have led to the initial formation of topography and rapid exhumation of gneissic rocks shortly after the metamorphic peak, followed by an outward jump of deformation and the accretion of outboard terranes, until the present-day collision with the Yakutat terrane led to final exhumation. The southeastern section however would have been located along the highly obliquely convergent part of the margin, where highly oblique transpressional motion would have led to slow, regular cooling and exhumation in what *Koons et al.* [2010] refer to as the "oblique orogen." The increased cooling and exhumation rate during the last ~5–10 Ma could be the result of the final collision of the Yakutat terrane with the margin. In our opinion, the different cooling and exhumation histories registered by the three different sections nicely reflect the existence of the Alaskan orocline at least since ~50 Ma and illustrates the effect of different obliquity during transpression on the cooling and exhumation histories of a region.

6. Conclusions

[49] The tectonic evolution of the CMC as presented in this study represents an example for the behavior of middle to lower crust along a variably oblique convergent

continental margin during a time span of ~60 Myr. The CMC area is characterized by three superimposed fabrics: D_1 is related to the accretion of sediments to the margin during oblique convergence, D_2 represents a short-lived, unusual event related to forces acting on the margin due to either the subduction of an oceanic spreading ridge and/or a plate tectonic reorganization, and D_3 is the result of a switch back to transpression due to oblique convergence. During the first phase of oblique convergence (D_1), a large-scale accretionary prism was built up, which was vertically thinned and thermally weakened during the D_2 event. Deformation and exhumation concentrated in this thermally weakened part during the subsequent renewed oblique convergence (D_3). During this phase of transpression, the more convergent western and central parts of the complex experienced rapid cooling and exhumation, leading to extrusion of parts of the gneiss zone which resulted in an overall fan shape of the complex. The more obliquely oriented southeastern part of the complex experienced slow and regular cooling and exhumation. Final exhumation is related to the Neogene collision of the outboard Yakutat terrane, which first caused slow exhumation from north to south in the western and central parts of the complex and then rapid exhumation of the southern and southeastern parts of the complex along semibrittle to brittle faults.

Appendix A: Analytical Techniques

A1. The $^{40}Ar/^{39}Ar$ Method

[50] Muscovite and biotite separates were obtained by crushing, sieving, short milling and magnetic separation of fist-sized hand specimens. The separates were then cleaned by handpicking under a binocular and only transparent, inclusion-free grains were selected. Grain size of the final separates was ~0.1–0.5 mm. The hand-picked separates were cleaned in distilled water in an ultrasonic bath. Approximately ~5 mg of each sample were packed into Al foil and stacked into a silica glass tube shielded by a 0.2 mm thick cadmium liner. Eight sample splits (each ~5 mg) of flux monitor GA-1550 biotite (K/Ar age 98.5 ± 0.8 1σ [*Spell and McDougall*, 2003]) were intercalated in regular intervals between the samples. K glass and CaF_2 salts were included in the tube in order to monitor interfering nuclear reactions on potassium and calcium. The whole tube was irradiated during 15 h in the core of the Oregon State University research reactor facility. Step heating experiments were conducted at the geochronology laboratory at the University of Florida. Samples were loaded into a Modifications Ltd Double vacuum resistance furnace. 14 and 16 heating steps from 600°–1350°C were conducted for muscovites and biotites, respectively, with total 15 min heating time per step. The extracted gas was expanded into a stainless steel cleanup line and purified with two 50 L/s SAES getters. Argon isotopes were measured using a MAP215-50 mass spectrometer in electron multiplier mode.

[51] The software ArArCALC version 2.4 [*Koppers*, 2002] was used for data reduction. Data were corrected for system blanks and mass discrimination. Detailed isotopic measurements can be found in Text S1 and Figures S1–S3. We report error-weighted plateau ages when more than three high-temperature heating steps containing >50% of the total released $^{39}Ar_K$ have a MSWD that is smaller than a statistical *t Student* distribution. If this is not the case, we report error plateau ages [*Koppers*, 2002]. Traditional calculation of plateau ages based on equation (17) of *Koppers* [2002] does only account for analytical uncertainty, uncertainty on the J value determination and uncertainty on the total decay constant of ^{40}K. In order to also consider uncertainties on the individual λ_e and $\lambda\beta$ decay constants, the $^{40}K/K$ abundance ratio, the actual measurement of the primary K/Ar standard and the intercalibration of secondary $^{40}Ar/^{39}Ar$ standards an alternative set of age equations has to be used [*Renne et al.*, 1998; *Min et al.*, 2000; *Scaillet*, 2000; *Koppers*, 2002; *Fraser et al.*, 2008]. We therefore applied the recalibration tool incorporated in ArArCALC which calculates plateau ages based on the equations of *Karner and Renne* [1998], *Renne et al.* [1998] and *Min et al.* [2000] which allow incorporating all internal and external errors. The physical constants used for recalculation are given by *Min et al.* [2000] and *Spell and McDougall* [2003]. Only those recalculated ages are reported in the diagrams, Table 1 and the text.

[52] The flux monitor J was determined based on a total of 29 heating steps on eight sample splits which were distributed over the whole irradiation tube. The obtained J values scatter considerably and no gradient was detected over the tube. From the 29 heating steps we excluded (1) the steps with the most scatter in isotopic ratio determination, (2) the steps with only very little gas and (3) some visually selected bad steps. We then used the remaining 13 heating steps to calculate an error weighted mean of J = 0.00369 ± 0.0001122 (±3.04%, 2σ, only analytical error considered following *Koppers* [2002]). All isotopic data are given in Data Sets S1 and S2.

A2. The Rb/Sr Isochron Method

[53] The biotite separates prepared for $^{40}Ar/^{39}Ar$ step heating experiments (section A1) were additionally purified by grinding in an agate mill in alcohol, sieving and magnetic separation. Whole rock powders were obtained by milling of ~3 cm^3 sized samples. Chemical sample preparation was performed at the Geological Survey of Austria in Vienna following the procedure described by *Sölva et al.* [2005]. Sample weights used for dissolution were about 200 mg for biotite and 100 mg for whole rock. Isotopic measurements were done at the Department of Geological Sciences at the University of Vienna. Spiked Rb ratios were measured at a Finnigan® MAT 262, whereas unspiked Sr ratios were analyzed at a ThermoFinnigan® Triton TI TIMS. Sr was run from Re double filaments, whereas Rb was evaporated from a Ta filament. On the ThermoFinnigan® Triton the $^{87}Sr/^{86}Sr$ ratio determined for the international standard NBS987 was 0.710248 ± 4 (n = 17). The error for the calculated $^{87}Rb/^{86}Sr$ ratios was taken as ±1% (2 sigma). Isochron age calculation was performed with Isoplot/Ex [*Ludwig*, 2003]. All isotopic data are given in Data Set S3.

A3. Fission Track Zircon Method

[54] Zircon grains were extracted by crushing, sieving, magnetic and heavy liquid separation, and finally handpicked. After mounting the zircons in PFA Teflon and polishing them, fossil fission tracks were revealed by etching in a eutectic mixture of NaOH/KOH at 210°C for 4 to

8 h. External synthetic mica detectors were firmly attached and, after irradiation, etched for 40 minutes in 40% HF at 20°C. Thermal neutron irradiation was performed at the German Technical University München in Garching (FRM-II reactor). Neutron flux was monitored using CN1 dosimeter glasses. All samples have been analyzed using the external detector method as described by *Naeser* [1976] and *Gleadow* [1981]. Ages were calculated using the zeta calibration method [*Hurford and Green*, 1983] with a zeta factor of 159 ± 3.6 using the software TRACKKEY 4.2.g [*Dunkl*, 2002]. Counting of fission tracks was carried out using a Zeiss Axio Imager A1m microscope equipped with an AUTOSCAN™ stage. Only grains with their prism planes parallel to the polished surface were used for age dating. All data are given in Data Set S4.

[55] **Acknowledgments.** Financial support by the Fonds zur Wissenschaftlichen Förderung FWF project P-19366 (to D. Gasser, E. Bruand, and K. Stüwe) and NSF grant EAR 0711105 (to T. Pavlis) is greatly acknowledged. C. Carson and J. D. Champagnac are thanked for help in the field. A. Koppers is thanked for help with the ArArCALC-software. J. Gifford is thanked for help in the ArAr-Lab at the University of Florida. From the University of Vienna we thank U. Klötzli and F. Biedermann for the help with mineral separation and M. Horschinegg for help with the Rb-Sr measurements. P. Claus and J. Claus are thanked for flying in the field. Two anonymous reviewers are thanked for their constructive reviews.

References

Abu-Alam, T. S., and K. Stüwe (2009), Exhumation during oblique transpression: The Feiran-Solaf region, Egypt, *J. Metamorph. Geol.*, *27*, 439–459, doi:10.1111/j.1525-1314.2009.00827.x.

Amato, J. M., and T. L. Pavlis (2010), Detrital zircon ages from the Chugach terrane, southern Alaska, reveal multiple episodes of accretion and erosion in a subduction complex, *Geology*, *38*, 459–462, doi:10.1130/G30719.1.

Atwater, T. (1989), Plate tectonic history of the northeast Pacific and western North America, in *The Eastern Pacific Ocean and Hawaii*, vol. N., *The Geology of North America*, edited by E. L. Winterer et al., pp. 21–72, Geol. Soc. of Am., Boulder, Colo.

Ayuso, R. A., P. J. Haeussler, D. C. Bradley, D. W. Farris, N. K. Foley, and G. A. Wandless (2009), The role of ridge subduction in determining the geochemistry and Nd-Sr-Pb isotopic evolution of the Kodiak batholith in southern Alaska, *Tectonophysics*, *464*, 137–163, doi:10.1016/j.tecto.2008.09.029.

Barker, F., G. L. Farmer, R. A. Ayuso, G. Plafker, and J. S. Lull (1992), The 50 Ma granodiorite of the eastern Gulf of Alaska: Melting in an accretionary prism in the forearc, *J. Geophys. Res.*, *97*, 6757–6778, doi:10.1029/92JB00257.

Barr, T. D., and F. A. Dahlen (1989), Brittle frictional mountain building: 2. Thermal structure and heat budget, *J. Geophys. Res.*, *94*, 3923–3947, doi:10.1029/JB094iB04p03923.

Berger, A. L., and J. A. Spotila (2008), Denudation and deformation in a glaciated orogenic wedge: The St. Elias orogen, Alaska, *Geology*, *36*, 523–526, doi:10.1130/G24883A.1.

Berger, A. L., J. A. Spotila, J. B. Chapman, T. L. Pavlis, E. Enkelmann, N. A. Ruppert, and J. T. Buscher (2008), Architecture, kinematics, and exhumation of a convergent orogenic wedge: A thermochronological investigation of tectonic-climatic interactions within the central St. Elias orogen, Alaska, *Earth Planet. Sci. Lett.*, *270*, 13–24, doi:10.1016/j.epsl.2008.02.034.

Bol, A. J., and H. Gibbons (1992), Tectonic implications of out-of-sequence faults in an accretionary prism, Prince William Sound, Alaska, *Tectonics*, *11*, 1288–1300, doi:10.1029/92TC01327.

Bol, A. J., and S. M. Roeske (1993), Strike-slip faulting and block rotation along the contact fault system, eastern Prince William Sound, Alaska, *Tectonics*, *12*, 49–62, doi:10.1029/92TC01324.

Booth-Rea, G., D. Klaeschen, I. Grevemeyer, and T. Reston (2008), Heterogeneous deformation in the Cascadia convergent margin and its relation to thermal gradient (Washington, NW USA), *Tectonics*, *27*, TC4005, doi:10.1029/2007TC002209.

Bradley, D. C., P. J. Haeussler, and T. M. Kusky (1993), Timing of Early Tertiary ridge subduction in southern Alaska, *U.S. Geol. Surv. Bull.*, *2068*, 163–177.

Bradley, D. C., R. Parrish, W. Clendenen, D. Lux, P. W. Layer, M. Heizler, and T. Donley (2000), New geochronological evidence for the timing of Early Tertiary ridge subduction in southern Alaska, *U.S. Geol. Surv. Prof. Pap.*, *1615*, 5–21.

Bradley, D. C., T. M. Kusky, P. J. Haeussler, R. Goldfarb, M. Miller, J. Dumoulin, S. W. Nelson, and S. Karl (2003), Geologic signature of Early Tertiary ridge subduction in Alaska, in *Geology of a Transpressional Orogen Developed During Ridge-Trench Interaction Along the North Pacific Margin*, edited by V. B. Sisson et al., *Spec. Pap. Geol. Soc. Am.*, *371*, 19–49.

Bruand, E. (2011), A petrological study of the Chugach Metamorphic Complex in southern Alaska, Ph.D. thesis, 204 pp., Dep. of Earth Sci., Univ. of Graz, Graz, Austria.

Bruand, E., D. Gasser, K. Stüwe, and O. Beyssac (2010), Metamorphism of the Chugach Metamorphic Complex, (Alaska): New pressure estimates question the ridge subduction context, *Geophys. Res. Abstr.*, *12*, 12,235.

Bruhn, R. L., T. L. Pavlis, G. Plafker, and L. Serpa (2004), Deformation during terrane accretion in the Saint Elias orogen, Alaska, *Geol. Soc. Am. Bull.*, *116*, 771–787, doi:10.1130/B25182.1.

Byrne, T. (1979), Late Paleocene demise of the Kula-Pacific spreading center, *Geology*, *7*, 341–344, doi:10.1130/0091-7613(1979)7<341:LPDOTK>2.0.CO;2.

Carlson, W. D., R. A. Donelick, and R. A. Ketcham (1999), Variability of apatite fission track annealing kinetics: I. Experimental results, *Am. Mineral.*, *84*, 1213–1223.

Coe, R. S., B. R. Globerman, P. W. Plumley, and G. A. Thrupp (1985), Paleomagnetic results from Alaska and their tectonic implications, in *Tectonostratigraphic Terranes of the Circum-Pacific Region*, *Earth Sci. Ser.*, vol. 1, edited by D. G. Howell, pp. 85–108, Am. Assoc. of Pet. Geol., Stanford, Calif.

Coe, R. S., B. R. Globerman, and G. A. Thrupp (1989), Rotation of central and southern Alaska in the Early Tertiary: Oroclinal bending by megakinking?, in *Paleomagnetic Rotations and Continental Deformation*, edited by C. Kissel and C. Laj, pp. 327–342, Kluwer Acad., Dordrecht, Netherlands.

Cowan, D. S. (2003), Revisiting the Baranof-Leech River hypothesis for Early Tertiary coastwise transport of the Chugach–Prince William terrane, *Earth Planet. Sci. Lett.*, *213*, 463–475, doi:10.1016/S0012-821X(03)00300-5.

Czeck, D. M., and P. J. Hudleston (2003), Testing models for obliquely plunging lineations in transpression: A natural example and theoretical discussion, *J. Struct. Geol.*, *25*, 959–982, doi:10.1016/S0191-8141(02)00079-2.

Dahl, P. S. (1996), The crystal-chemical basis for Ar retention in micas: Inferences from interlayer partitioning and implications for geochronology, *Contrib. Mineral. Petrol.*, *123*, 22–39, doi:10.1007/s004100050141.

Dickinson, W. R. (2009), Anatomy and global context of the North American Cordillera, in *Backbone of the Americas: Shallow Subduction, Plateau Uplift, and Ridge and Terrane Collision*, edited by S. M. Kay et al., *Mem. Geol. Soc. Am.*, *204*, 1–29.

Dodson, M. H. (1973), Closure temperature in cooling geochronological and petrological systems, *Contrib. Mineral. Petrol.*, *40*, 259–274, doi:10.1007/BF00373790.

Doubrovine, P. V., and J. A. Tarduno (2008), A revisited kinematic model for the relative motion between Pacific oceanic plates and North America since the Late Cretaceous, *J. Geophys. Res.*, *113*, B12101, doi:10.1029/2008JB005585.

Dunkl, I. (2002), Trackkey: A Windows program for calculation and graphical presentation of fission track data, *Comput. Geosci.*, *28*, 3–12, doi:10.1016/S0098-3004(01)00024-3.

Dunlap, W. J. (1997), Neocrystallization or cooling? $^{40}Ar/^{39}Ar$ ages of white micas from low-grade mylonites, *Chem. Geol.*, *143*, 181–203, doi:10.1016/S0009-2541(97)00113-7.

Dusel-Bacon, C. (1994), Metamorphic history of Alaska, in *The Geology of Alaska*, vol. G-1, *The Geology of North America*, edited by G. Plafker and H. C. Berg, pp. 495–533, Geol. Soc. of Am., Boulder, Colo.

Engebretson, D. C., A. Cox, and R. G. Gordon (1985), Relative motions between oceanic and continental plates in the Pacific basin, *Spec. Pap. Geol. Soc. Am.*, *206*, 1–59.

Enkelmann, E., J. I. Garver, and T. L. Pavlis (2008), Rapid exhumation of ice-covered rocks of the Chugach–St. Elias orogen, southeast Alaska, *Geology*, *36*, 915–918, doi:10.1130/G2252A.1.

Enkelmann, E., P. K. Zeitler, T. L. Pavlis, J. I. Garver, and K. D. Ridgway (2009), Intense localized rock uplift and erosion in the St Elias orogen of Alaska, *Nat. Geosci.*, *2*, 360–363, doi:10.1038/ngeo502.

Enkelmann, E., P. K. Zeitler, J. I. Garver, T. L. Pavlis, and B. P. Hooks (2010), The thermochronological record of tectonic and surface process interaction at the Yakutat–North American collision zone in southeast Alaska, *Am. J. Sci.*, *310*, 231–260, doi:10.2475/04.2010.01.

Farmer, G. L., R. Ayuso, and G. Plafker (1993), A Coast Mountains provenance for the Valdez and Orca groups, southern Alaska, based on Nd, Sr and Pb isotopic evidence, *Earth Planet. Sci. Lett.*, *116*, 9–21, doi:10.1016/0012-821X(93)90042-8.

Farris, D. W., and S. R. Paterson (2009), Subduction of a segmented ridge along a curved continental margin: Variations between the western and eastern Sanak-Baranof belt, southern Alaska, *Tectonophysics*, *464*, 100–117, doi:10.1016/j.tecto.2007.10.008.

Farris, D. W., P. Haeussler, R. Friedman, S. Paterson, R. W. Saltus, and R. Ayuso (2006), Emplacement of the Kodiak batholith and slab-window migration, *Geol. Soc. Am. Bull.*, *118*, 1360–1376, doi:10.1130/B25718.1.

Fisher, D. M., and T. Byrne (1992), Strain variations in an ancient accretionary complex: Implications for forearc evolution, *Tectonics*, *11*, 330–347, doi:10.1029/91TC01490.

Forster, M. A., and G. S. Lister (2008), Tectonic sequence diagrams and the structural evolution of schists and gneisses in multiply deformed terranes, *J. Geol. Soc.*, *165*, 923–939, doi:10.1144/0016-76492007-016.

Fossen, H., and B. Tikoff (1993), The deformation matrix for simultaneous simple shearing, pure shearing and volume change, and its application to transpression-transtension tectonics, *J. Struct. Geol.*, *15*, 413–422, doi:10.1016/0191-8141(93)90137-Y.

Foster, D. A., B. D. Goscombe, and D. R. Gray (2009), Rapid exhumation of deep crust in an obliquely convergent orogen: The Kaoko Belt of the Damara Orogen, *Tectonics*, *28*, TC4002, doi:10.1029/2008TC002317.

Fraser, G. L., K. Hussey, and D. M. Compston (2008), Timing of Paleoproterozoic Au-Cu-Bi and W-mineralization in the Tennant Creek region, northern Australia: Improved constraints via intercalibration of $^{40}Ar/^{39}Ar$ and U-Pb ages, *Precambrian Res.*, *164*, 50–65, doi:10.1016/j.precamres.2008.03.005.

Fuis, G. S., and G. Plafker (1991), Evolution of deep structure along the Trans-Alaska Crustal Transect, Chugach Mountains and Copper River Basin, southern Alaska, *J. Geophys. Res.*, *96*, 4229–4253, doi:10.1029/90JB02276.

Fuis, G. S., et al. (2008), Trans-Alaska Crustal Transect and continental evolution involving subduction underplating and synchronous foreland thrusting, *Geology*, *36*, 267–270, doi:10.1130/G24257A.1.

Gasser, D. (2010), Evolution of the Chugach Metamorphic Complex of southern Alaska in space and time, Ph.D. thesis, 315 pp., Dep. of Earth Sci., Univ. of Graz, Graz, Austria.

Gleadow, A. J. W. (1981), Fission-track dating methods: What are the real alternatives?, *Nucl. Tracks*, *5*, 3–14, doi:10.1016/0191-278X(81)90021-4.

Goscombe, B. D., and D. R. Gray (2009), Metamorphic response in orogens of different obliquity, scale and geometry, *Gondwana Res.*, *15*, 151–167, doi:10.1016/j.gr.2008.07.005.

Green, P. F., I. R. Duddy, A. J. W. Gleadow, P. R. Tingate, and G. M. Laslett (1986), Thermal annealing of fission tracks in apatite 1. A qualitative description, *Chem. Geol.*, *59*, 237–253, doi:10.1016/0168-9622(86)90074-6.

Groome, W. G., and D. J. Thorkelson (2009), The three-dimensional thermo-mechanical signature of ridge subduction and slab window migration, *Tectonophysics*, *464*, 70–83, doi:10.1016/j.tecto.2008.07.003.

Haeussler, P. J., D. Bradley, R. Goldfarb, L. Snee, and C. Taylor (1995), Link between ridge subduction and gold mineralization in southern Alaska, *Geology*, *23*, 995–998, doi:10.1130/0091-7613(1995)023<0995:LBRSAG>2.3.CO;2.

Haeussler, P. J., D. C. Bradley, R. E. Wells, and M. L. Miller (2003), Life and death of the Resurrection plate: Evidence for its existence and subduction in the northeastern Pacific in Paleocene-Eocene time, *Geol. Soc. Am. Bull.*, *115*, 867–880, doi:10.1130/0016-7606(2003)115<0867:LADOTR>2.0.CO;2.

Haeussler, P. J., G. E. Gehrels, and S. M. Karl (2005), Constraints on the age and provenance of the Chugach accretionary complex from detrital zircons in the Sitka Graywacke near Sitka, Alaska, in *Studies by the U.S. Geological Survey in Alaska, 2004*, edited by P. J. Haeussler and J. P. Galloway, *U.S. Geol. Surv. Prof. Pap.*, *1709-F*, 1–11.

Harris, N. R., V. B. Sisson, J. E. Wright, and T. L. Pavlis (1996), Evidence for Eocene mafic underplating during fore-arc intrusive activity, eastern Chugach mountains, Alaska, *Geology*, *24*, 263–266, doi:10.1130/0091-7613(1996)024<0263:EFEMUD>2.3.CO;2.

Harrison, T. M., J. Célérier, A. B. Aikman, J. Hermann, and M. T. Heizler (2009), Diffusion of ^{40}Ar in muscovite, *Geochim. Cosmochim. Acta*, *73*, 1039–1051, doi:10.1016/j.gca.2008.09.038.

Hill, M., J. Morris, and J. Whelan (1981), Hybrid granodiorites intruding the accretionary prism, Kodiak, Shumagin, and Sanak Islands, southwest Alaska, *J. Geophys. Res.*, *86*, 10,569–10,590, doi:10.1029/JB086iB11p10569.

Hudson, T., and G. Plafker (1982), Paleogene metamorphism of an accretionary flysch terrane, eastern Gulf of Alaska, *Geol. Soc. Am. Bull.*, *93*, 1280–1290, doi:10.1130/0016-7606(1982)93<1280:PMOAAF>2.0.CO;2.

Hudson, T., G. Plafker, and M. A. Lanphere (1977a), Intrusive rocks of the Yakutat–St. Elias area, south-central Alaska, *J. Res. U.S. Geol. Surv.*, *5*, 155–172.

Hudson, T., G. Plafker, and M. A. Lanphere (1977b), Metamorphic rocks of the Yakutat–St. Elias area, south-central Alaska, *J. Res. U.S. Geol. Surv.*, *5*, 173–184.

Hudson, T., G. Plafker, and Z. E. Peterman (1979), Paleogene anatexis along the Gulf of Alaska margin, *Geology*, *7*, 573–577, doi:10.1130/0091-7613(1979)7<573:PAATGO>2.0.CO;2.

Hurford, A. J., and P. F. Green (1983), The zeta age calibration of fission track dating, *Isot. Geosci.*, *1*, 285–317.

Jenkin, G. R. T. (1997), Do cooling paths derived from mica Rb-Sr data reflect true cooling paths?, *Geology*, *25*, 907–910, doi:10.1130/0091-7613(1997)025<0907:DCPDFM>2.3.CO;2.

Jones, R. R., R. E. Holdsworth, and W. Bailey (1997), Lateral extrusion in transpression zones: The importance of boundary conditions, *J. Struct. Geol.*, *19*, 1201–1217, doi:10.1016/S0191-8141(97)00034-5.

Jones, R. R., R. E. Holdsworth, P. Clegg, K. McCaffrey, and E. Tavarnelli (2004), Inclined transpression, *J. Struct. Geol.*, *26*, 1531–1548, doi:10.1016/j.jsg.2004.01.004.

Karner, D. B., and R. P. Renne (1998), $^{40}Ar/^{39}Ar$ geochronology of Roman volcanic province tephra in the Tiber river valley: Age calibration of middle Pleistocene sea-level changes, *Geol. Soc. Am. Bull.*, *110*, 740–747, doi:10.1130/0016-7606(1998)110<0740:AAGORV>2.3.CO;2.

Koons, P. O., R. J. Norris, D. Craw, and A. F. Cooper (2003), Influence of exhumation on the structural evolution of transpressional plate boundaries: An example from the southern Alps, New Zealand, *Geology*, *31*, 3–6, doi:10.1130/0091-7613(2003)031<0003:IOEOTS>2.0.CO;2.

Koons, P. O., B. P. Hooks, T. Pavlis, P. Upton, and A. D. Barker (2010), Three-dimensional mechanics of Yakutat convergence in the southern Alaskan plate corner, *Tectonics*, *29*, TC4008, doi:10.1029/2009TC002463.

Koppers, A. (2002), ArArCALC—Software for $^{40}Ar/^{39}Ar$ age calculations, *Comput. Geosci.*, *28*, 605–619, doi:10.1016/S0098-3004(01)00095-4.

Little, T. A., and C. W. Naeser (1989), Tertiary tectonics of the Border Ranges fault system, Chugach Mountains, Alaska: Deformation and uplift in a forearc setting, *J. Geophys. Res.*, *94*, 4333–4359, doi:10.1029/JB094iB04p04333.

Lonsdale, P. (1988), Paleogene history of the Kula plate: Offshore evidence and onshore implications, *Geol. Soc. Am. Bull.*, *100*, 733–754, doi:10.1130/0016-7606(1988)100<0733:PHOTKP>2.3.CO;2.

Ludwig, K. R. (2003), *Isoplot/Ex Version 3.0: A Geochronological Toolkit for Microsoft Excel*, 70 pp., Berkeley Geochronol. Cent. Spec. Publ., Berkeley, Calif.

Lull, J. S., and G. Plafker (1990), Geochemistry and paleotectonic implications of metabasaltic rocks in the Valdez Group, southern Alaska, in *Geological Studies in Alaska by the U.S. Geological Survey, 1989*, edited by J. H. Dover and J. P. Galloway, *U.S. Geol. Surv. Bull.*, *1946*, 29–38.

Lytwyn, J., S. Lockhart, J. Casey, and T. Kusky (2000), Geochemistry of near-trench intrusives associated with ridge subduction, Seldovia Quadrangle, southern Alaska, *J. Geophys. Res.*, *105*, 27,957–27,978, doi:10.1029/2000JB900294.

Madsen, J. K., D. J. Thorkelson, R. M. Friedman, and D. D. Marshall (2006), Cenozoic to recent plate configurations in the Pacific Basin: Ridge subduction and slab window magmatism in western North America, *Geosphere*, *2*, 11–34, doi:10.1130/GES00020.1.

Marshak, R. S., and D. E. Karig (1977), Triple junctions as a cause for anomalously near-trench igneous activity between the trench and volcanic arc, *Geology*, *5*, 233–236, doi:10.1130/0091-7613(1977)5<233:TJAACF>2.0.CO;2.

McAleer, R. J., J. A. Spotila, E. Enkelmann, and A. L. Berger (2009), Exhumation along the Fairweather fault, southeastern Alaska, based on low-temperature thermochronometry, *Tectonics*, *28*, TC1007, doi:10.1029/2007TC002240.

McDougall, I., and T. M. Harrison (1999), *Geochronology and Thermochronology by the $^{40}Ar/^{39}Ar$ Method*, 2nd ed., 269 pp., Oxford Univ. Press, New York.

Meigs, A., S. Johnston, J. Garver, and J. Spotila (2008), Crustal-scale structural architecture, shortening, and exhumation of an active, eroding wedge (Chugach/St Elias Range, southern Alaska), *Tectonics*, *27*, TC4003, doi:10.1029/2007TC002168.

Min, K., R. Mundil, P. R. Renne, and K. Ludwig (2000), A test for systematic errors in $^{40}Ar/^{39}Ar$ geochronology through comparison with U/Pb analysis of a 1.1-Ga rhyolite, *Geochim. Cosmochim. Acta*, *64*, 73–98, doi:10.1016/S0016-7037(99)00204-5.

Naeser, C. W. (1976), Fission-track dating, *U.S. Geol. Surv. Open File Rep., 76-190*, 1–65.

Nilsen, T. H., and G. G. Zuffa (1982), The Chugach terrane: A Cretaceous trench-fill deposit, southern Alaska, in *Trench-Forearc Geology: Sedimentation and Tectonics on Modern and Active Plate Margins*, edited by J. K. Laggett, pp. 213–227, Blackwell Sci., Oxford, U. K.

Nokleberg, W. J., G. Plafker, J. S. Lull, W. K. Wallace, and G. R. Winkler (1989), Structural analysis of the southern Peninsular, southern Wrangellia,

and northern Chugach terranes along the Trans-Alaska Crustal Transect, northern Chugach Mountains, Alaska, *J. Geophys. Res.*, *94*, 4297–4320, doi:10.1029/JB094iB04p04297.

Norton, I. O. (1995), Plate motions in the North Pacific: The 43 Ma nonevent, *Tectonics*, *14*, 1080–1094, doi:10.1029/95TC01256.

Oldow, J. S., A. W. Bally, H. G. A. Lallemant, and W. P. Leeman (1989), Phanerozoic evolution of the North American Cordillera: United States and Canada, in *The Geology of North America—An Overview*, edited by A. W. Bally and A. R. Palmer, pp. 139–232, Geol. Soc. of Am., Boulder, Colo.

Onstott, T. C., V. B. Sisson, and D. L. Turner (1989), Initial argon in amphiboles from the Chugach Mountains, southern Alaska, *J. Geophys. Res.*, *94*, 4361–4372, doi:10.1029/JB094iB04p04361.

O'Sullivan, P. B., G. Plafker, and J. M. Murphy (1997), Apatite fission-track thermotectonic history of crystalline rocks in the northern Saint Elias Mountains, Alaska, in *Geological Studies in Alaska by the U.S. Geological Survey, 1995*, edited by J. A. Dumoulin and J. E. Gray, *U.S. Geol. Surv. Prof. Pap.*, *1574*, 283–293.

Pavlis, T. L., and S. M. Roeske (2007), The Border Range fault system, in *Tectonic Growth of a Collisional Continental Margin: Crustal Evolution of Southern Alaska*, edited by K. D. Ridgway et al., *Spec. Pap. Geol. Soc. Am.*, *431*, 95–128.

Pavlis, T. L., and V. B. Sisson (1995), Structural history of the Chugach metamorphic complex in the Tana River region, eastern Alaska: A record of Eocene ridge subduction, *Geol. Soc. Am. Bull.*, *107*, 1333–1355, doi:10.1130/0016-7606(1995)107<1333:SHOTCM>2.3.CO;2.

Pavlis, T. L., and V. B. Sisson (2003), Development of a subhorizontal decoupling horizon in a transpressional system, Chugach Metamorphic Complex, Alaska: Evidence for rheological stratification of the crust, in *Geology of a Transpressional Orogen Developed During Ridge-Trench Interaction Along the North Pacific Margin*, edited by V. B. Sisson et al., *Spec. Pap. Geol. Soc. Am.*, *371*, 191–216.

Pavlis, T. L., C. Picornell, L. Serpa, R. L. Bruhn, and G. Plafker (2004), Tectonic processes during oblique collision: Insights from the St. Elias orogen, northern North American Cordillera, *Tectonics*, *23*, TC3001, doi:10.1029/2003TC001557.

Philpotts, A. R., and J. J. Ague (2009), *Principles of Igneous and Metamorphic Petrology*, 2nd ed., 667 pp., Cambridge Univ. Press, Cambridge, U. K.

Plafker, G., J. C. Moore, and G. R. Winkler (1994), Geology of the southern Alaska margin, in *The Geology of Alaska*, vol. G-1, *The Geology of North America*, edited by G. Plafker and H. C. Berg, pp. 389–449, Geol. Soc. of Am., Boulder, Colo.

Reiners, W. R., Z. Zhou, T. A. Ehlers, C. Xu, M. T. Brandon, R. A. Donelick, and S. Nicolescu (2003), Post-orogenic evolution of the Dabie Shan, eastern China, from (U-Th)/He and fission track thermochronology, *Am. J. Sci.*, *303*, 489–518, doi:10.2475/ajs.303.6.489.

Renne, P. R., C. C. Swisher, A. L. Deino, D. B. Karner, T. L. Owens, and D. J. DePaolo (1998), Intercalibration of standards, absolute ages and uncertainties in $^{40}Ar/^{39}Ar$ dating, *Chem. Geol.*, *145*, 117–152, doi:10.1016/S0009-2541(97)00159-9.

Robin, P.-Y. F., and A. R. Cruden (1994), Strain and vorticity patterns in ideally ductile transpression zones, *J. Struct. Geol.*, *16*, 447–466, doi:10.1016/0191-8141(94)90090-6.

Roeske, S. M., L. W. Snee, and T. L. Pavlis (2003), Dextral-slip reactivation of an arc-forearc boundary during Late Cretaceous–Early Eocene oblique convergence in the northern Cordillera, in *Geology of a Transpressional Orogen Developed During Ridge-Trench Interaction Along the North Pacific Margin*, edited by V. B. Sisson et al., *Spec. Pap. Geol. Soc. Am.*, *371*, 141–169.

Sample, J. C., and M. R. Reid (2003), Large-scale, latest Cretaceous uplift along the northeast Pacific Rim: Evidence from sediment volume, sandstone petrography, and Nd isotopic signatures of the Kodiak Formation, Kodiak Islands, Alaska, in *Geology of a Transpressional Orogen Developed During Ridge-Trench Interaction Along the North Pacific Margin*, edited by V. B. Sisson et al., *Spec. Pap. Geol. Soc. Am.*, *371*, 51–70.

Sanderson, D. J., and W. R. D. Marchini (1984), Transpression, *J. Struct. Geol.*, *6*, 449–458, doi:10.1016/0191-8141(84)90058-0.

Scaillet, S. (2000), Numerical error analysis in $^{40}Ar/^{39}Ar$ dating, *Chem. Geol.*, *162*, 269–298, doi:10.1016/S0009-2541(99)00149-7.

Scharman, M. R., T. L. Pavlis, E. M. Day, and L. J. O'Driscoll (2011), Deformation and structure in the Chugach Metamorphic Complex, southern Alaska: Crustal architecture of a transpressional system from a down-plunge section, *Geosphere*, in press.

Schulmann, K., A. B. Thompson, O. Lexa, and J. Ježek (2003), Strain distribution and fabric development modeled in active and ancient transpressive zones, *J. Geophys. Res.*, *108*(B1), 2023, doi:10.1029/2001JB000632.

Sisson, V. B., and L. S. Hollister (1988), Low-pressure facies series metamorphism in an accretionary sedimentary prism, southern Alaska, *Geology*, *16*, 358–361, doi:10.1130/0091-7613(1988)016<0358:LPFSMI>2.3.CO;2.

Sisson, V. B., and T. L. Pavlis (1993), Geologic consequences of plate reorganization: An example from the Eocene southern Alaska fore-arc, *Geology*, *21*, 913–916, doi:10.1130/0091-7613(1993)021<0913:GCOPRA>2.3.CO;2.

Sisson, V. B., L. S. Hollister, and T. C. Onstott (1989), Petrologic and age constraints on the origin of a low-pressure/high-temperature metamorphic complex, southern Alaska, *J. Geophys. Res.*, *94*, 4392–4410, doi:10.1029/JB094iB04p04392.

Sisson, V. B., A. R. Poole, N. R. Harris, H. C. Burner, P. Copeland, A. D. Raymond, and W. C. McLelland (2003), Geochemical and geochronologic constraints for genesis of a tonalite-trondhjemite suite and associated mafic intrusive rocks in the eastern Chugach Mountains, Alaska: A record of ridge transform subduction, in *Geology of a Transpressional Orogen Developed During Ridge-Trench Interaction Along the North Pacific Margin*, edited by V. B. Sisson et al., *Spec. Pap. Geol. Soc. Am.*, *371*, 293–326.

Sölva, H., B. Grasemann, M. Thöni, R. Thiede, and G. Habler (2005), The Schneeberg normal fault zone: Normal faulting associated with Cretaceous SE-directed extrusion in the eastern Alps (Italy/Austria), *Tectonophysics*, *401*, 143–166, doi:10.1016/j.tecto.2005.02.005.

Spell, T. L., and I. McDougall (2003), Characterization and calibration of $^{40}Ar/^{39}Ar$ dating standards, *Chem. Geol.*, *198*, 189–211, doi:10.1016/S0009-2541(03)00005-6.

Spotila, J. A., J. T. Buscher, A. J. Meigs, and P. W. Reiners (2004), Long-term glacial erosion of active mountain belts: Example of the Chugach–St. Elias Range, Alaska, *Geology*, *32*, 501–504, doi:10.1130/G20343.1.

Teyssier, C., and B. Tikoff (1999), Fabric stability in oblique convergence and divergence, *J. Struct. Geol.*, *21*, 969–974, doi:10.1016/S0191-8141(99)00067-X.

Teyssier, C., B. Tikoff, and M. Markley (1995), Oblique plate motion and continental tectonics, *Geology*, *23*, 447–450, doi:10.1130/0091-7613(1995)023<0447:OPMACT>2.3.CO;2.

Thompson, A. B., K. Schulmann, and J. Jezek (1997), Thermal evolution and exhumation in obliquely convergent (transpressive) orogens, *Tectonophysics*, *280*, 171–184, doi:10.1016/S0040-1951(97)00144-3.

Tikoff, B., and C. Teyssier (1994), Strain modelling of displacement-field partitioning in transpressional orogens, *J. Struct. Geol.*, *16*, 1575–1588, doi:10.1016/0191-8141(94)90034-5.

Trop, J. M., and K. D. Ridgway (2007), Mesozoic and Cenozoic tectonic growth of southern Alaska: A sedimentary perspective, in *Tectonic Growth of a Collisional Continental Margin: Crustal Evolution of Southern Alaska*, edited by K. D. Ridgway et al., *Spec. Pap. Geol. Soc. Am.*, *431*, 55–94.

Villa, I. (1998), Isotopic closure, *Terra Nova*, *10*, 42–47, doi:10.1046/j.1365-3121.1998.00156.x.

Wagner, G., and P. van den Haute (1992), *Fission-Track Dating*, 285 pp., Enke Verlag, Stuttgart, Germany.

Wallace, W. K., and D. C. Engebretson (1984), Relationships between plate motions and Late Cretaceous to Paleogene magmatism in southwestern Alaska, *Tectonics*, *3*, 295–315, doi:10.1029/TC003i002p00295.

Whitney, D. L., and B. W. Evans (2010), Abbreviation for names of rock-forming minerals, *Am. Mineral.*, *95*, 185–187, doi:10.2138/am.2010.3371.

Whitney, D. L., C. Teyssier, and M. T. Heizler (2007), Gneiss domes, metamorphic complexes, and wrench zones: Thermal and structural evolution of the Niğde Massif, central Anatolia, *Tectonics*, *26*, TC5002, doi:10.1029/2006TC002040.

Wolf, R. A., K. A. Farley, and L. T. Silver (1996), Helium diffusion and low temperature thermochronometry of apatite, *Geochim. Cosmochim. Acta*, *60*, 4231–4240, doi:10.1016/S0016-7037(96)00192-5.

Zumsteg, C. L., G. R. Himmelberg, S. Karl, and P. Haeussler (2003), Metamorphism within the Chugach accretionary complex on Baranof island, southeastern Alaska, in *Geology of a Transpressional Orogen Developed During Ridge-Trench Interaction Along the North Pacific Margin*, edited by V. B. Sisson et al., *Spec. Pap. Geol. Soc. Am.*, *371*, 253–267.

E. Bruand, D. Gasser, and K. Stüwe, Department of Earth Science, University of Graz, Universitätsplatz 2, A-8010 Graz, Austria. (emilie.bruand@uni-graz.at; deta.gasser@geo.uio.no; kurt.stuewe@uni-graz.at)

D. A. Foster, Department of Geological Sciences, University of Florida, 241 Williamson Hall, PO Box 112120, Gainesville, FL 32611, USA. (dafoster@ufl.edu)

B. Fügenschuh, Faculty of Geo- and Atmospheric Sciences, University of Innsbruck, Innrain 52, A-6020 Innsbruck, Austria.

T. Pavlis, Department of Geological Sciences, University of Texas at El Paso, Geology 405, 500 West University Blvd., El Paso, TX 79968, USA. (pavlis@geo.utep.edu)

R. Schuster, Geological Survey of Austria, Neulinggasse 38, A-1030 Vienna, Austria. (ralf.schuster@geologie.ac.at)